minerals

MDPI

Article

Provenance and Uranium Sources in the Lower Cretaceous Huanhe Formation of Northern Ordos Basin: Constraints from Detrital Zircon U–Pb Geochronology and Hf Isotopes

Xin Zhang [1,2,*], Junfan Che [1,2], Fengjun Nie [1,2,*], Aisheng Miao [3], Zhaobin Yan [1], Chengyong Zhang [1] and Yujie Hu [3]

[1] State Key Laboratory of Nuclear Resources and Environment, East China University of Technology, Nanchang 330013, China; 18779481127@163.com (J.C.)
[2] School of Earth Sciences, East China University of Technology, Nanchang 330013, China
[3] Nuclear Industry Co., Ltd., Baotou 014000, China
* Correspondence: zhangxin@ecut.edu.cn (X.Z.); 198460002@ecut.edu.cn (F.N.)

Abstract

The Ordos Basin is a key district for sandstone-hosted uranium, yet host-rock controls and uranium sources remain debated. We integrate measured sections, whole-rock geochemistry, and detrital zircon U-Pb-Lu-Hf data from the Cretaceous Huanhe Formation (Yihewusu, northern Ordos) to resolve provenance, transport, and enrichment pathways. Uranium enrichment is concentrated in feldspathic-lithic sandstones deposited in proximal fluvial-lacustrine settings. Detrital zircon ages define three clusters—Phanerozoic (500–200 Ma), Paleoproterozoic (2000–1700 Ma), and Neoarchean (2600–2300 Ma)—with Proterozoic grains >60%, indicating derivation from Archean–Paleoproterozoic TTG gneisses, granulites, and khondalites of the Yinshan Block and the northern Central Orogenic Belt. Zircon εHf(t) values (−10.84 to +7.76) and crustal model ages (3.2–2.1 Ga) record substantial Meso- to Neoarchean crustal growth in the source terranes. Critically, Permian-Cretaceous intermediate-felsic igneous rocks along the northern margin of the Western North China Block—marked by elevated U, Th/U > 5 (indicative of U loss), pervasive feldspar microfractures, and proximity to basin-margin uranium belts—are identified as the principal uranium reservoirs. We propose a dual uranium supply: soluble uranium mobilized from leached igneous rocks during weathering and fluid-rock interaction, and U-enriched detritus delivered to the basin. Uranium concentrated in redox-sensitive, feldspathic-lithic sandstones of the Huanhe Formation, which effectively trapped advected uranium at proximal facies transitions. These findings establish a direct genetic link between basin-margin uranium sources and in-basin mineralization, providing a predictive framework for regional uranium exploration in North China.

Keywords: Ordos Basin; Huanhe Formation; U-Pb dating; Hf isotope; provenance

check for updates

Academic Editor: Urs Klötzli

Received: 17 September 2025
Revised: 12 October 2025
Accepted: 13 October 2025
Published: 16 October 2025

Citation: Zhang, X.; Che, J.; Nie, F.; Miao, A.; Yan, Z.; Zhang, C.; Hu, Y. Provenance and Uranium Sources in the Lower Cretaceous Huanhe Formation of Northern Ordos Basin: Constraints from Detrital Zircon U–Pb Geochronology and Hf Isotopes. *Minerals* **2025**, *15*, 1079. https://doi.org/10.3390/min15101079

Copyright: © 2025 by the authors. Licensee MDPI, Basel, Switzerland. This article is an open access article distributed under the terms and conditions of the Creative Commons Attribution (CC BY) license (https://creativecommons.org/licenses/by/4.0/).

1. Introduction

Sandstone-hosted uranium mineralization represents one of the predominant forms of uranium deposits globally [1,2]. These deposits typically originate either during sedimentation itself or through subsequent diagenesis [1,3]. Consequently, understanding the characteristics of the host rock formations—including their facies, depositional age, and origin—is crucial for unraveling the formation processes of sediment-hosted uranium deposits.

Over nearly four decades, geologists have identified sandstone-type uranium deposits within six Mesozoic-Cenozoic sedimentary basins in northern China: the Yili, Tuha,

Bayingobi, Ordos, Erlian, and Songliao basins [4–8]. Among these, the Ordos Basin contains the richest uranium resources [9,10]. As a key multi-energy basin in northern China, the Ordos Basin hosts significant deposits of coal, uranium, oil, and natural gas. Its formation is closely tied to the tectonic activities of three major structural domains: the Paleo-Asia, Tethys, and Circum-Pacific [11,12]. The northwestern part of the basin, situated between the Yimeng Uplift and Tianhuan syncline, has experienced multiple intense tectonic phases. These complex movements hinder the determination of sediment provenance and introduce significant uncertainties in predicting sandstone-type uranium reservoirs within the basin [13–15]. Detrital sediments are vital for deciphering sedimentary basin tectonic backgrounds, intracontinental basin evolution, and characterizing source rock properties [16–18].

In the northern segment of the Ordos Basin, substantial uranium deposits including large-scale and super large sandstone-type ones like Dongsheng, Nalinggou, Daying, and Hantaimiao have been uncovered. Meanwhile, smaller deposits such as Shuanglong, Diantou, and Guojiawan are distributed in the south [19]. Moreover, this sedimentary basin is endowed with substantial energy reserves, encompassing fossil fuels like coal, petroleum, and natural gas, which are pivotal for regional energy resource inventories [20]. Within the Ordos Basin, the majority of uranium-bearing strata belong to the Middle Jurassic Zhiluo Formation. A notable example is the Dongsheng uranium deposit [21]. The strata of the Zhiluo Formation, characterized by extensive distribution, a high width-to-thickness ratio, and broad-ranging connectivity, are likely to create advantageous conditions for the movement and accumulation of ore-carrying fluids [22]. Moreover, significant uranium resources have been detected in the Cretaceous strata of the basin. Notable occurrences are in the northern Yihewusu region and the southern Zhengyuan area [23,24]. Numerous investigations have been carried out regarding sediment sources and the tectonic evolutionary history of the northern Ordos Basin. These efforts have amassed substantial geological, geochemical, and chronological datasets [25,26]. Nonetheless, the origin of uranium, the source of sediments in the Cretaceous ore-bearing target layer, and their connection to uranium mineralization processes are yet to be fully elucidated.

Studying the geochemistry of clastic sediments offers insights into the evolution of both the basin and surrounding mountains [27,28]. Sediments deposited in the basin represent eroded products from geological bodies of the surrounding highlands. As they are partially or completely eroded, accumulated sediments in the basin are the only clues we need to reconstruct the region's tectonic evolution. Therefore, we intended to carry out systematic petrological, geochemical, and chronological investigations on the Huanhe Formation, a significant ore-hosting layer spanning the northern expanse of the Ordos Basin. We combined our findings with previous data to determine the formation, evolution history, and uranium source conditions of the uranium-ore-bearing target strata.

2. Regional Geological Setting

2.1. Ordos Basin

Part of the western North China Plate (106–111° E and 35–40° N), the Ordos Basin covers approximately 2.5×10^5 km^2 and is a Mesozoic-Cenozoic inland depression basin evolved from the Paleozoic stable craton background of the Ordos Plate [29,30]. Exhibiting a sub-rectangular shape and a north-northeast orientation, the basin is surrounded by a succession of fault zones, fault basins, and orogenic belts. Specifically, the Daqingshan-Wulashan lies to its north, the Qilian-Qinling-Kunlun orogenic zone extends along its southern margin, and the Lvliang and Alxa Blocks span from its eastern to western flanks [31,32]. The Ordos Basin undergoes multi-stage tectonic evolution, as shown in Figure 1. The

red-framed area represents the Yihewusu study region, and the red star marks the sampling location at ZKY0–31 drill hole (Figure 1b).

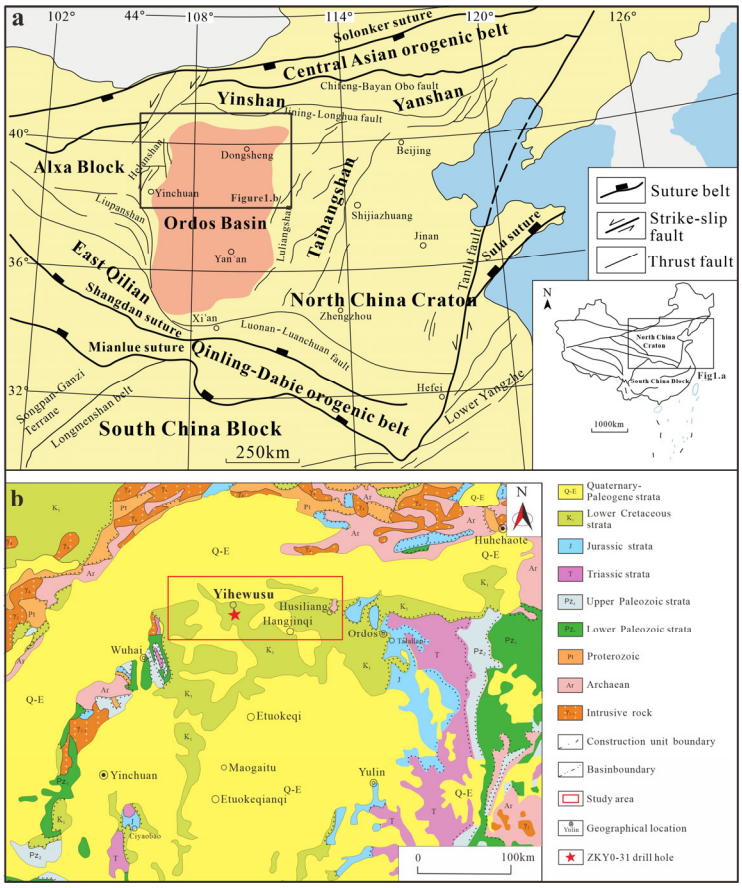

Figure 1. (**a**) Location of the Ordos Basin in the simplified tectonic map of the North China Craton and its adjacent regions (modified from Zhong et al. [33]); (**b**) Regional geological map and tectonic setting of the Ordos Basin (modified from Wang et al. [34]).

The basin's formation was governed by multiple significant tectonic events, including the Caledonian, Indosinian, and Yanshanian orogenies. The tectonic evolution produced diverse basin types: a terminal Proterozoic aulacogen, an early Paleozoic paralic basin, a Late Carboniferous intracratonic basin, a Late Triassic to Early Cretaceous residual craton basin, and a Cenozoic marginal fault basin [35,36]. Within the Mesozoic strata (Triassic, Jurassic, and Early Cretaceous epochs), the Middle Jurassic Zhiluo Formation (J_2z) is the most important uranium-bearing rock system [7,33]. The surface of the study area is mostly covered by loess of the Quaternary (Q). Thick Meso-Cenozoic strata are developed. According to the geological age from old to new, the sequence of strata is as follows: the Triassic (T), including the Yanchang Formation (T_3y) of the Upper Triassic, the Zhifang Formation (T_2z) of the Middle Triassic, the Heshanggou Formation (T_1h) and the Liujiagou Formation (T_1l) of the Lower Triassic; the Fuxian Formation (J_1f) of the Lower Jurassic, the Yanan Formation (J_2y), the Zhiluo Formation (J_2z) and the Anding Formation (J_2a) of the Middle Jurassic; the Luohe Formation (K_1l), the Huanhe Formation (K_1h), the Luohandong Formation (K_1lh) and the Jinchuan Formation (K_1j) of the Lower Cretaceous; the Upper Pliocene of the Neogene (N_2); and the Quaternary (Q) (corresponding to the stratigraphic sequence shown in Figure 2) [37]. We confirmed the Luohe Formation (K_1l), Huanhe Formation (K_1h), and Luohandong Formation (K_1lh) of the Lower Cretaceous as new uranium-bearing rock series (Figure 2). The Huanhe Formation and the Jingchuan

Formation are primarily lacustrine delta depositional systems, characterized by mainly lakes in the basin hinterland, while the basin margin is mainly deltaic deposition [34].

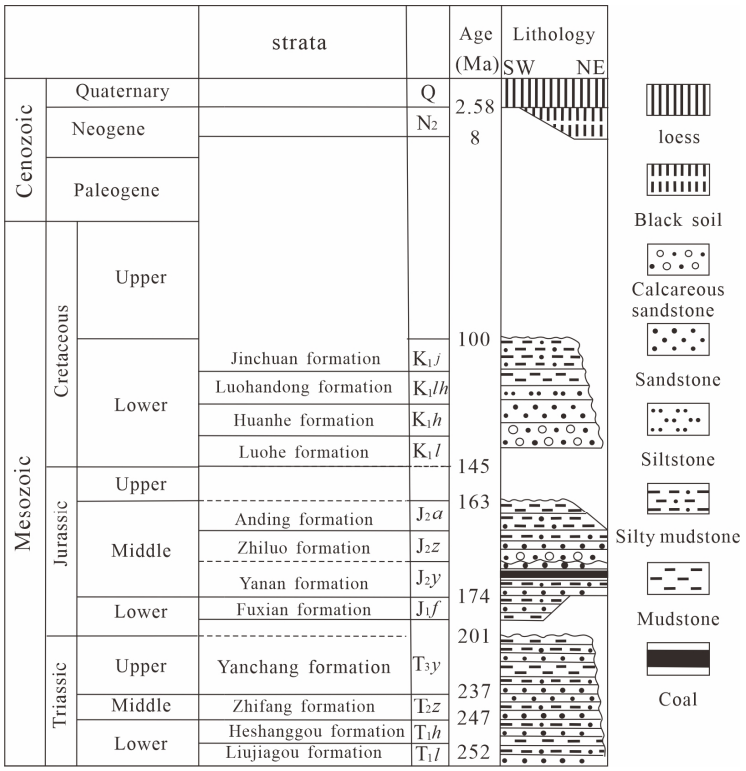

Figure 2. Lithology of strata in the Ordos Basin (Revised by Wang et al. [34]).

2.2. Geological Background of the Study Area

The Ordos Basin, situated in the western part of the North China Craton, is a large superimposed basin developed on a stable continental block. Its formation and evolution have undergone intricate tectono-sedimentary cycles spanning hundreds of millions of years through multiple episodes [38,39]. During the Archean-Early Paleoproterozoic, the North China Craton experienced multiple phases of tectonic activity, leading to the amalgamation and consolidation of continental nuclei. The Lvliang Movement around 1800 Ma finally cratonized the basement, forming a rigid crystalline basement composed of granulite and greenschist-facies metamorphic rocks. By the end of the Mesoproterozoic (approximately 1000 Ma), the Grenville orogenic event caused the closure of surrounding oceanic basins, incorporating the North China Block into the Rodinia supercontinent. During the Neoproterozoic, the breakup of the Rodinia supercontinent led to the redevelopment of passive continental margins along the southern and northern edges of the basin [13,40].

At the end of the Early Paleozoic, the Caledonian orogeny triggered bidirectional subduction of the Qin-Qi Ocean and Xingmeng Ocean, resulting in the overall uplift of the basin and a depositional hiatus for Silurian-Devonian strata. In the Late Paleozoic, the basin entered a marine-continental transitional stage, with the sedimentary environment shifting from marine facies to fluvial-deltaic systems [14,41]. Influenced by the Indosinian Movement, the North China Plate fragmented, and the Ordos region west of the Taihang Mountains formed an independent intracontinental basin. During the Late Jurassic-Early Cretaceous, the subduction of the Pacific Plate induced lithospheric thinning and increased heat flow. This tectonic-thermal event not only drove hydrocarbon generation from source rocks. Affected by the Himalayan Movement, the basin has been continuously uplifted and subjected to denudation since the Late Cretaceous. Concurrently, a series of rift basins,

such as the Hetao, Yinchuan basins, developed around the periphery of the Ordos Basin, accumulating thick sedimentary sequences [31,32,40].

NEE-trending or nearly NE-trending faults are well-developed in the northern part of the Ordos Basin, primarily including the Sanyanjing Fault, Wulanjilinmiao Fault, and Boerjianghaizi Fault (Figure 3). The three faults are connected by two transform slopes, forming a left-step en echelon shape. The western section trends east–west, changing to a northeast–southwest direction towards the east. These faults cut through the Middle Jurassic Yan'an Formation, Zhiluo Formation, Upper Jurassic Anding Formation, Lower Cretaceous Luohe Formation, and Huanhe Formation. They can supply abundant reducing gases to the Lower Cretaceous, which form a reducing barrier and facilitate the subsequent uranium mineralization [42]. The Huanhe Formation (K_1h) represents a key ore-hosting stratum in this region, with an estimated formation age of approximately 141–135 Ma. Vertically, it exhibits a red oxidation zone in the upper part, a red and green interlayer transition zone in the middle, and a green and gray reduction zone in the lower part [33]. Uranium mineralization predominantly occurs in the strata of the middle transition zone within the Huanhe Formation. Ore composition is complex, with uranium stone being the primary uranium mineral. Uranium minerals commonly manifest as irregular colloidal masses that precipitate along the peripheries of detrital grains or infill the fractures within detrital particles. A significant quantity of uranium minerals also deposit around the margins of pyrite with minute grains [42,43]. The Huanhe Formation transitions from a braided river delta plain in the north to a delta front and prodelta toward the south. High-quality uranium reservoirs are formed by large-scale (subaqueous) braided distributary channel sand bodies. Uranium mineralization mainly develops along the front edge of braided river deltas, where large uranium reservoir sand bodies enter the lake [43].

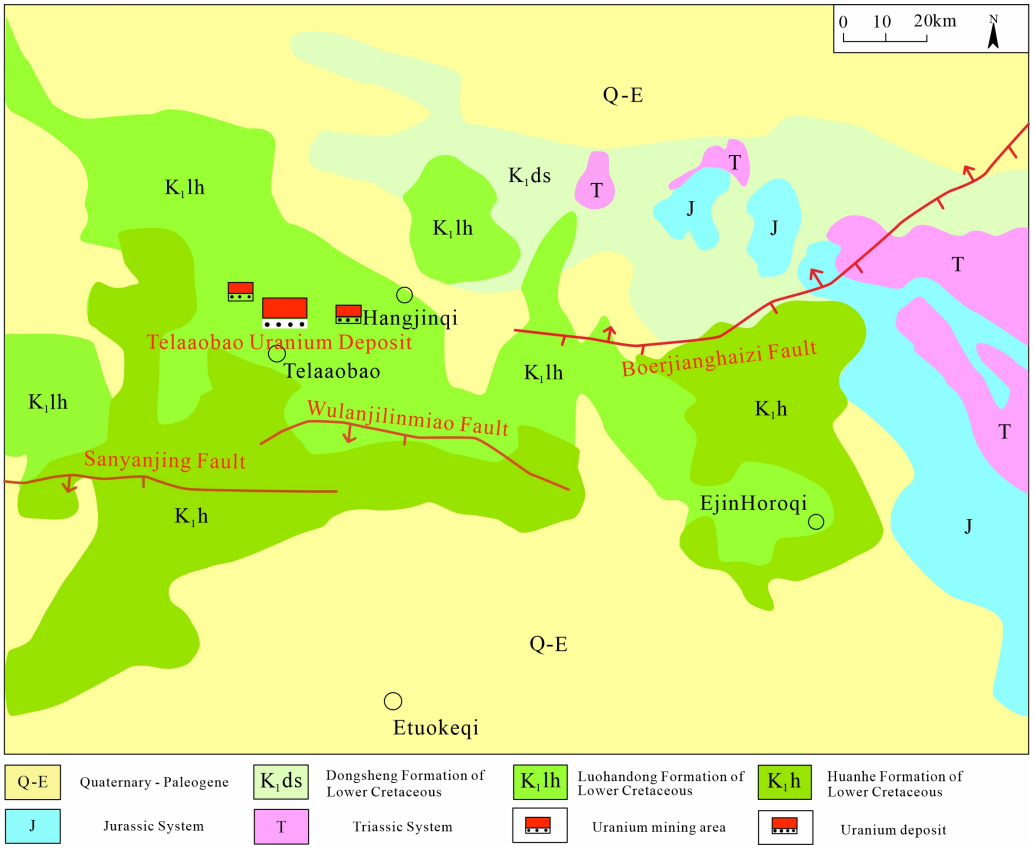

Figure 3. Geological map of northern Ordos basin (Revised by Wang et al. [42]).

3. Sampling and Methods

3.1. Sample Collection

In the Yihewusu area of the northwestern Ordos Basin, ten sandstone samples were collected from the Huanhe Formation of drill hole ZKY0-31 (Figure 1) and utilized for zircon chronology and Hf isotope analysis. Sampling depths spanned 145.6 m to 654.8 m, targeting key intervals of the Huanhe Formation critical for uranium-bearing sedimentary analysis.

3.2. Rare Earth Element

The whole-rock trace element analysis was conducted at ALS Environmental (Guangzhou, China) Co., Ltd. Trace elements were determined using ICP-MS. Rare earth element (REE) analyses of the sandstone samples from the Huanhe Formation were performed using inductively coupled plasma mass spectrometry (ICP-MS) on a Thermo Fisher X Series II quadrupole instrument (Thermo Fisher Scientific, Waltham, MA, USA). For the instrument operation, the radiofrequency power was set at 1300 W, the sampling depth at 8 mm, and the nebulizer gas flow rate at 0.8 L/min, with a mass scanning range of 5–250 amu and a dwell time of 50 ms per peak in peak-jumping mode. Sample preparation followed an acid digestion procedure: the samples were first pulverized to 200 mesh and dried at 105 °C for 3 h. Exactly 50 ± 1 mg of powder was weighed into a polytetrafluoroethylene (PTFE) digestion vessel and subjected to stepwise dissolution with high-purity HNO_3, HF, and $HClO_4$. After complete digestion, an internal standard solution of Rh was added, and the mixture was diluted to a final weight of 100.0 g with deionized water, resulting in a Rh concentration of 10 ng/mL. The analytical precision for all elements was better than 5%.

To guarantee data credibility, samples from the Huanhe Formation were analyzed in parallel with internationally acknowledged geochemical reference materials (CRMs). These CRMs encompass NIST SRM 1646a [44] (an estuarine sediment standard from the National Institute of Standards and Technology in the USA) and GSD-12 [45] (a shale standard from the Institute of Geophysical and Geochemical Exploration, Chinese Academy of Geological Sciences, China). For NIST SRM 1646a, the measured concentrations of key rare earth elements (REEs), such as La (35.1 ± 1.0 μg/g) and Ce (78.3 ± 2.2 μg/g), exhibited a high degree of consistency with the certified values, with relative deviations (RD) less than 3%. Correspondingly, for GSD-12, the measured values of Sm (5.97 ± 0.20 μg/g) and Yb (2.84 ± 0.09 μg/g) were in close alignment with their certified counterparts, and the relative deviations (RD) were below 2.5%. The analytical precision for all REEs in our samples, quantified by the relative standard deviation (RSD), was superior to 5%. This meets the quality control requirements for trace element analysis in geological samples, as specified by international standards like ISO 11466:1995 [46] (Soil quality-Guidelines for the collection and handling of soil quality data).

3.3. Zircon LA-ICP-MS Chronology and Hf Isotope Analysis

Zircon sample selection was completed at Langfang Chengxin Mine Testing Technology. Zircon with large particles and well-developed crystal forms was selected as targets under binoculars, then captured with cathodoluminescence (CL) and transreflection photography. The State Key Laboratory of Nuclear Resources and Environment at East China University of Technology carried out zircon U-Pb dating. A GeoLasHD laser ablation system (Coherent, Göttingen, Germany) featuring a 193 nm ArF excimer laser was employed for this purpose. An Agilent 7900 inductively coupled plasma mass spectrometer (ICP-MS) was utilized for the analysis. The laser was set with a 30 μm beam spot diameter, an energy density of 10 J/cm^2, and an ablation frequency of 10 Hz. The 91,500 standard was employed as the isotopic age reference, while the international standard sample SRM610 [47]

served for elemental content calibration of the U, Th, and Pb concentrations. Common Pb calibration was carried out based on the measured ^{204}Pb values. Data processing was accomplished using Glitter 1.6.6 and ICPMSDataCal 9.0 software. Zircon U-Pb age concordia diagrams were constructed, and weighted mean age calculations were performed using Isoplot 3.0 software.

For the analysis of Hf isotope composition, zircon grains exhibiting a higher degree of concordance were chosen. This analysis, which was integrated with the zircon U-Pb age test, was completed at Wuhan Shangshu Science and Technology. The test was performed with the NWR193HE (Version 3.0) laser ablation system (carrier gas: He, laser beam diameter: 44 μm, ablation frequency: 8 Hz) and the Neptune Plus (Version 1.0) multi-collector plasma mass spectrometer (LA-MC-ICP-MS). A zircon standard (e.g., 91500, Plesovice, Temora, or GJ-1) was employed as the monitoring standard sample. During analysis, the weighted average of ^{176}Hf/^{177}Hf for GJ-1 was 0.282007 ± 0.000025 (2σ). The decay constant of Lu employed for calculating the initial ^{176}Hf/^{177}Hf ratio was 1.865 × 10^{-11}a^{-1}. Zircon εHf(t) values were calculated according to U-Pb ages. The calculations used chondrite Hf isotope ^{176}Lu/^{177}Hf and ^{176}Hf/^{177}Hf values of 0.0336 and 0.282785, respectively. For the determination of the single-stage zircon Hf model age (T_{DM1}), a mantle-derived depleted component ^{176}Hf/^{177}Hf ratio of 0.282325 and ^{176}Lu/^{177}Lu ratio of 0.0384 were utilized. The two-stage zircon Hf model age (T_{DM2}) was computed according to an average crustal ^{176}Lu/^{177}Hf ratio of 0.015.

4. Results

4.1. Field Observations

Sandstone from the west Atamu area of Yihewusu exhibited trough-shaped cross-bedding and an iron combination (limonite) (Figure 4A,B). Rock formations in the Arbas Sumu area were variegated sandstone with trough-shaped cross-bedding, locally containing gray-white calcareous nodules and purple mudstone lenses at the bottom (Figure 4C,D). The Sumitu Aobao area exhibited thin mudstone layers interbedded with yellowish-green, medium-grained sandstone. In southeast Yihewusu, at Hongqing River Town, the variegated coarse sandstone contained rust-colored patches (Figure 4E,F).

The Huanhe Formation is subdivided into an upper and lower segment (K_1h^1, K_1h^2). In the interval from 654.8 to 145.6 m, ripple-bearing and planar-laminated sandstone units are interbedded with thinner-bedded laminated mudstone and minor siltstone intervals, developing fining-upward cyclic sequences (Figure 5).

4.2. Petrographic Analysis

Sandstone detritus mainly comprised quartz and feldspar, followed by lithic fragments. Iron-bearing materials were observable in the underlying section of the Huanhe Formation, while a variety of heavy minerals were detected across the entire formation (Figure 6). Microscopic observation revealed >90% composition of rock particles, predominantly quartz and feldspar, with black lithic fragments visible. The sandstone exhibited strong cementation and strong resistance to weathering. Quartz content ranged from 20% to 75%, feldspar from 15% to 60%, and lithic fragments from 10% to 30%. Overall sorting was poor, with semi-automorphic, angular to sub-angular grains. Filling materials were mainly mud cement and carbonate cement, with matrix minerals including illite, sericite, and kaolinite. Heavy minerals were rare, mainly magnetite, ilmenite, and garnet. Mica and asphalt strips filled in gaps between the grains, with some mica being squeezed and deformed by particles.

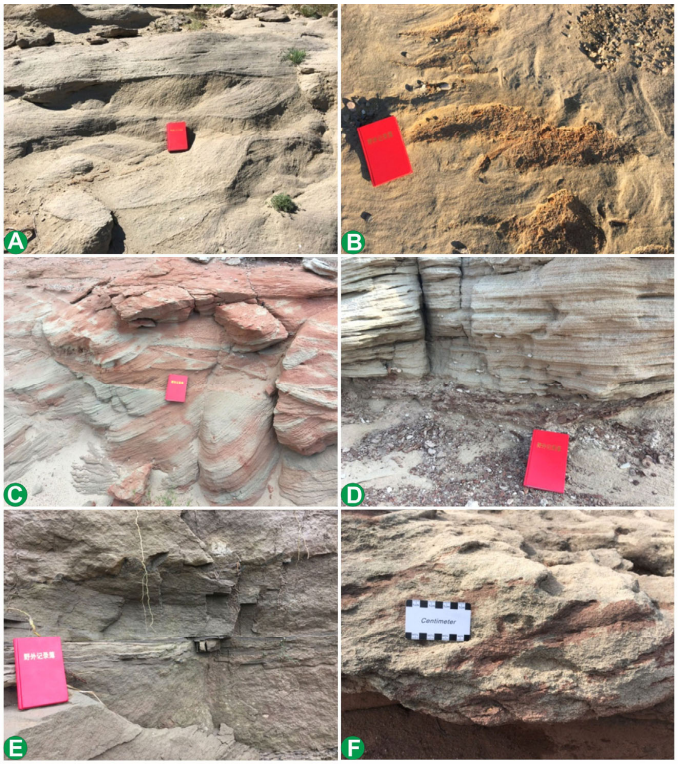

Figure 4. Field photographs of Huanhe Formation in west Atamu of Yihewusu, from the northern Ordos Basin. (**A**) Trough cross-bedding developed in gray-white medium sandstone from west Atamu of Yihewusu. (**B**) Iron nodules developed in yellow coarse sandstone from west Atamu of Yihewusu. (**C**) Variegated sandstone with trough cross-bedding from Arbasi Sumu. (**D**) Gray sandstone (with gray-white calcareous nodules) from Arbasi Sumu, with purple mudstone lenses visible at bottom. (**E**) Yellow-green medium sandstone interbedded with thin mudstone from Sumitu Aobao. (**F**) Variegated coarse sandstone of Hongqinghe Town southeast of Yihewusu.

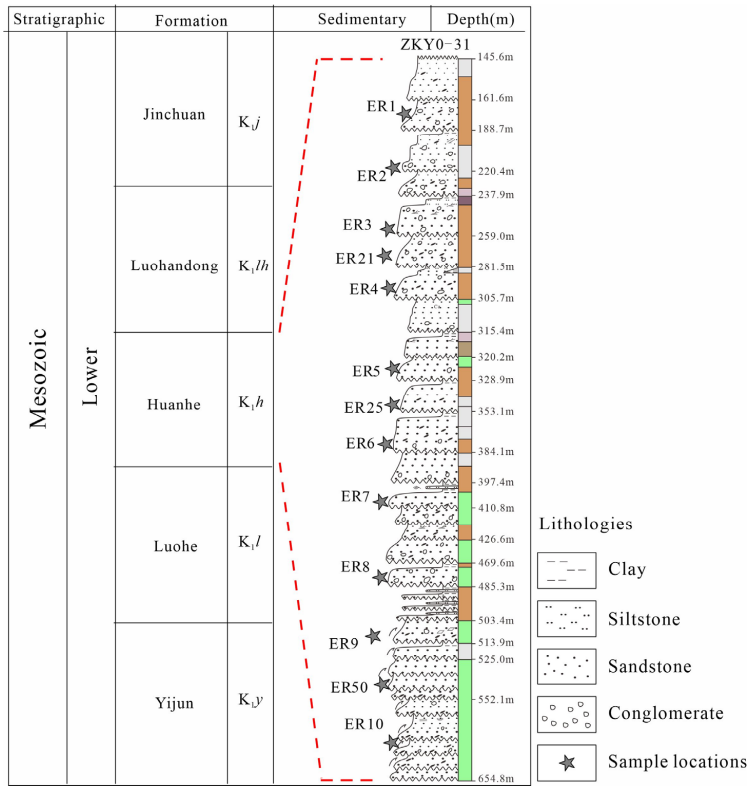

Figure 5. Stratigraphic Summary of ZKY0-31 Drill Core, with Sample Depth Annotations.

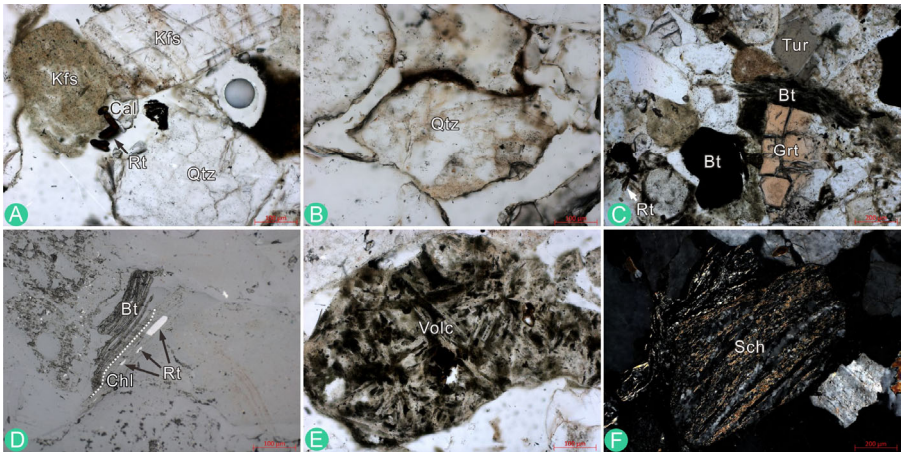

Figure 6. Microscopic characteristics of detrital composition in Huanhe Formation sandstone. (**A**) Debris particles included potassium feldspar (Kfs) and quartz (Qtz), with rutile (Rt) and calcite cement (Cal) at the edges of the particles. ZKW2020-1, 415.14 m, 200× (single polarized light). (**B**) Quartz (Qtz) with iron impregnation at the edge. ZKW2020–1411, 20 m, 200× (single polarized light). (**C**) Shaped columnar rutile (Rt), block-shaped asphalt (Bit), light red garnet with two sets of fissures (Grt), biotite (Bt), light brown tourmaline (Tur). ZKW2020–1401, 64 m, 100× (single polarized light). (**D**) Biotite (Bt) contains rutile (Rt) in the cleavage joint, with some chloritization (Chl) in the biotite. ZKW2020–1415, 14 m, 200× (reflected light). (**E**) Volcanic rock debris (Volc), mainly comprising interlaced thin lath plagioclase and matrix ejected rock debris, with weak optical property of the matrix and interfill structure. ZKW2020–1415, 14 m, 200× (monochromatic). (**F**) Schist rock debris (Sch), mainly composed of quartz and sericite, arranged in a continuous and directional manner, forming a sheet-like structure. ZKW2020–1411, 20 m, 100× (orthogonal polarization).

4.3. Rare Earth Elements

Table A1 lists REE data for sandstone samples. Total REEs (∑REE) ranged from 59.23 to 1422.13 × 10^{-6} and averaged 425.57 × 10^{-6}. The ranges of light and heavy REEs (LREE, HREE) were 49.12–1383.93 × 10^{-6} and 5.66–38.2 × 10^{-6}, respectively, averaging 405.13 × 10^{-6} and 12.46 × 10^{-6}. LREE/HREE ratios varied between 4.86 and 36.23 (average 17.69), indicating LREE enrichment, HREE depletion, and notable fractionation between the two groups. Leveraging the widely accepted chondrite-normalized data [44], a rare earth element (REE) distribution pattern was constructed (Figure 7a). REE distribution curves normalized to chondrite showed a clear right-hand inclination and a typical V-shaped configuration (Figure 7a). The parallelism of REE distribution curves across samples suggested synchronous variation in REE content. The North American Shale Composite (NASC)-normalized REE pattern is nearly flat to slightly right-sloping (Figure 7b).

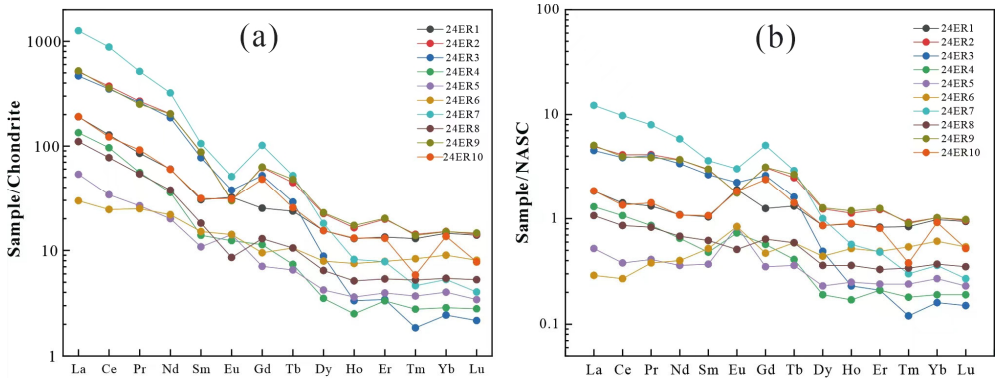

Figure 7. (**a**) Chondrite-normalized REE distribution pattern in Yihewusu area [48] and (**b**) North American shale-normalized (NASC) REE distribution pattern in Yihewusu area.

4.4. Detrital Zircon U-Pb Dating Results

Zircon grains in the sandstone samples predominantly exhibited short columnar and rounded shapes, as shown in CL images, with some retaining long columnar morphology and others having sharp edges. The majority of zircon grains exhibited Th/U ratios exceeding 0.4, a characteristic signature diagnostic of magmatic origin, as documented in Table A2. Zircon particle size varied greatly (range: 100–200 μm), with some grains being severely damaged. Most zircon particles developed oscillating rings or plate-like zones (Figure 8).

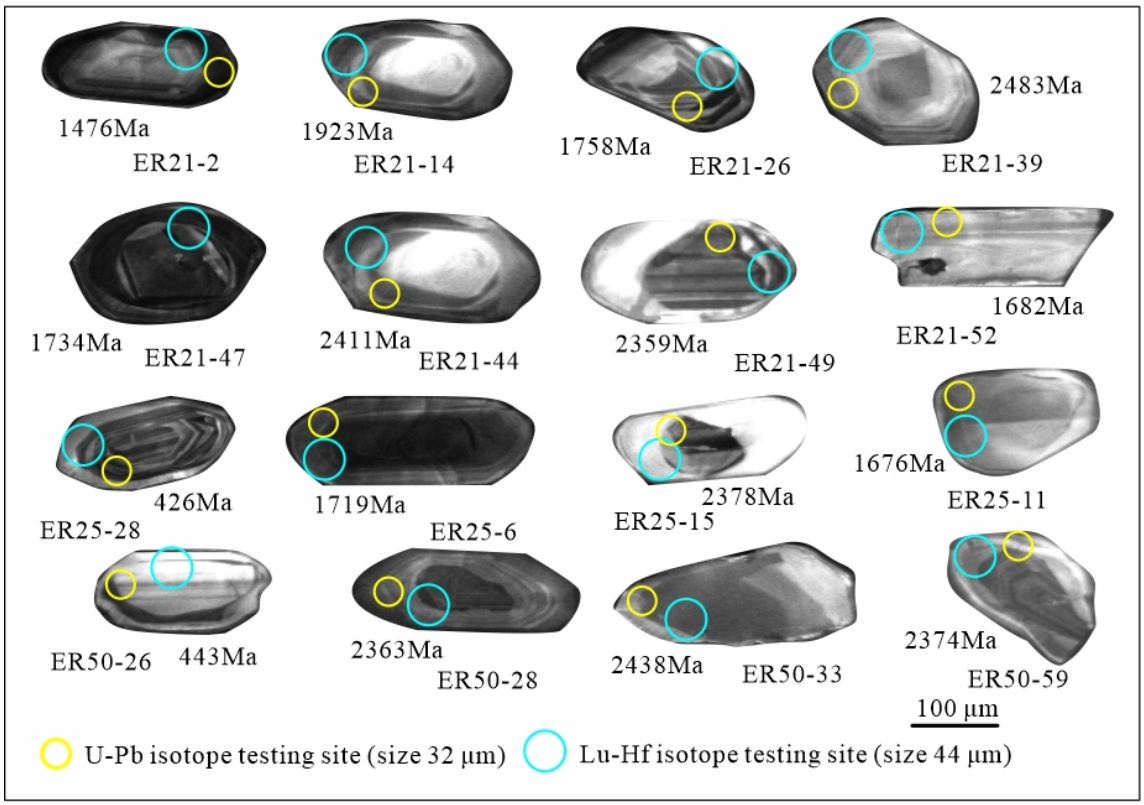

Figure 8. Cathodoluminescence (CL) Imaging of Representative Sedimentary Rocks from the Huanhe Formation.

This experiment analyzed 280 detrital zircon grains and obtained 248 valid U-Pb age combinations (concordant rate >90%, Table A2). The U-Pb ages of zircon displayed a broad distribution, roughly spanning from 200 Ma to 2800 Ma, and could be categorized into three distinct clusters, 300–500 Ma, 1700–2000 Ma, and 2300–2600 Ma, as illustrated in the detrital zircon age histograms of Figure 9.

For ER21 zircon samples, 81 data points with concordant degree >90% were selected for analysis. Zircon Th content was 20×10^{-6}–881×10^{-6}, and the U content was 18×10^{-6}–1340×10^{-6}. The Th/U ratios predominantly exceeded 0.1, spanning a range from 0.10 to 4.00, as shown in Table A2.

For ER25 zircon samples, 86 data points with concordant degree >90% were selected for analysis. Th content ranged from 25×10^{-6} to 802×10^{-6}, and U content ranged from 30×10^{-6} to 892×10^{-6}. All Th/U ratios were greater than 0.1, fluctuating within the range of 0.10–1.70, as detailed in Table A2.

For ER50 zircon samples, 81 data points with concordant degree >90% were selected for analysis. Zircon Th content ranged from 8×10^{-6} to 877×10^{-6}, while U content

ranged from 15 × 10^{-6} to 1456 × 10^{-6}. The Th/U ratios of zircon grains presented values exceeding 0.1, with a range spanning from 0.10 to 2.30, as tabulated in Table A2.

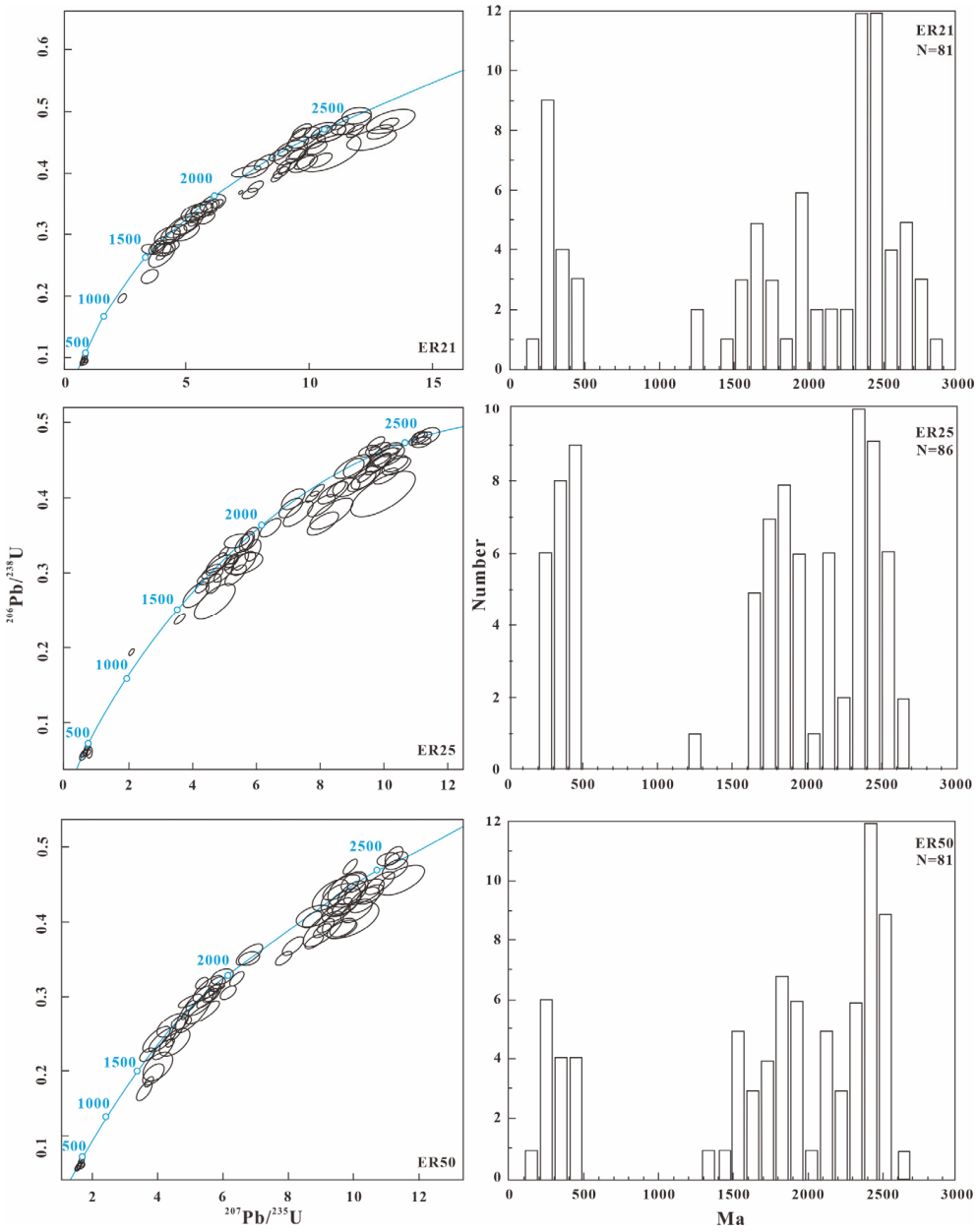

Figure 9. U-Pb Geochronology of Detrital Zircons from Huanhe Formation Metasedimentary Rocks: Concordia Diagrams, Weighted Ages, and Frequency Histograms.

To avoid the influence of lead loss on dating accuracy, the $^{207}Pb/^{206}Pb$ age of zircon older than 1000 Ma was used. For zircon less than 1000 Ma, the $^{206}Pb/^{238}U$ age was used instead. The U-Pb age Concordia diagrams of detrital zircon (Figure 9) indicated that U-Pb age fell on or near the harmonic line and the data points predominantly cluster within three age intervals, 200–500 Ma, 1700–2000 Ma, and 2300–2600 Ma, forming prominent age peaks.

4.5. Hf Isotope Composition of Detrital Zircons

Hf isotope analysis was conducted on 88 detrital zircons, yielding 86 valid data points (Table A3, Figure 10), co-located with or morphologically similar to the specimens selected for LA-ICP-MS U-Pb dating. This figure presents our detrital zircon data from the Huanhe

Formation, plotted against the CHUR-DM reference model following the methodology of earlier research [49–54]. Zircon grains ranged from positive to negative εHf(t) and were categorized into three groups. The oldest (ca. 2300–2600 Ma) had εHf(t) values that varied between 4.11 and −8.34 epsilon units. A cluster of younger zircon grains (ca. 1800–2000 Ma) possessed predominately negative εHf(t) values falling to −10.84, characteristic of crustal material sources. The youngest zircon group (ca. 300–500 Ma) had εHf(t) range of −1.85 to −10.78 epsilon units.

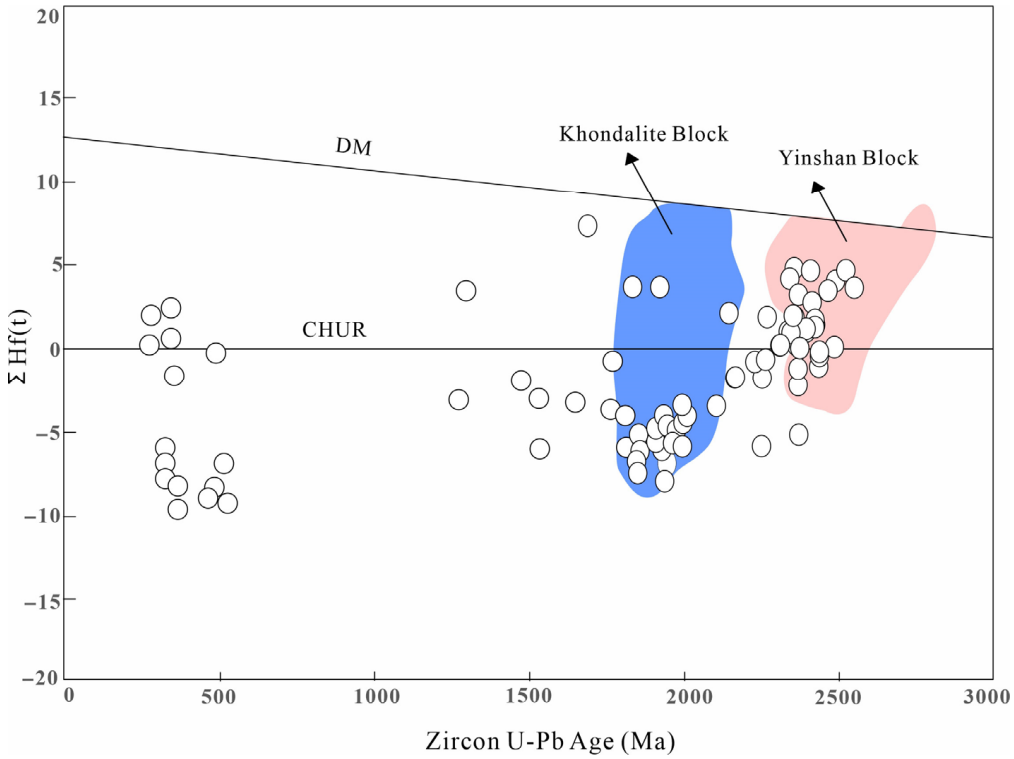

Figure 10. Correlation between Initial εHf(t) and U-Pb Ages of Detrital Zircons in the Huanhe Formation. All circles shown are results of our analyses. CHUR denotes the homogeneous chondrite-like reservoir, while DM represents the depleted mantle, which is constructed based on the contemporary average values of $^{176}Hf/^{177}Hf = 0.28325$ and $^{176}Lu/^{177}Hf = 0.0334$. Khondalite Block and Yinshan Block are tectonic units as provenances (elaborated above).

The Khondalite Block and Yinshan Block are important tectonic units in the study area. The Khondalite Block is a typical tectonic-lithological unit, which preserves records of ancient tectonic-thermal events and can provide detrital materials with specific geochemical characteristics [55]. The Yinshan Block acts as a related provenance, contributing some zircons formed by the recycling of ancient crust [56]. In Figure 10, the distribution ranges of εHf(t) and zircon U-Pb ages of detrital zircons in the Huanhe Formation are clearly delineated. These distribution characteristics can effectively trace the material input pattern of different provenances to the Huanhe Formation. Among them, both the Khondalite Block and the Yinshan Block are identified as major provenance tectonic units. Further observation reveals that the distribution density of zircon data points within and around the area corresponding to the Yinshan Block is relatively higher, suggesting that in the provenance supply of this sedimentary system, the contribution of the Yinshan Block may be more prominent, while the contribution scale from source areas for the Khondalite Block is potentially limited.

5. Discussion

5.1. Provenance of Detrital Zircon

The North China Craton (NCC), among the most ancient cratons globally, consists of a continental core exceeding 3.0 Ga and multiple micro-terranes. These terranes amalgamated during a crustal growth episode spanning 2.9–2.7 Ga. The craton has a multistage, complex structural evolution history, including large-scale magmatic and metamorphic events at 2.5 Ga, Paleoproterozoic orogeny events at 2.3–1.9 Ga, basement uplift after 1.8 Ga, as well as other continental rift and non-orogenic magmatic events [57,58]. The western domain of the NCC has a more limited exposure of basement and is characterized by higher stability, encompassing regions such as Ji'ning, Daqingshan, Guyang Wuchuan, Serteng, Helanshan Qilianshan, and Alxa. It is mainly composed of metamorphic crystalline complexes from the Neoarchean and Early Proterozoic [59].

In Yihewusu, sandstone has relatively low detrital zircon content from the Neoproterozoic, accounting for 4.6% of total zircon. These ages are comparable to the 2.6–2.5 Ga TTG gneiss, mafic-ultramafic layered intrusions, and crustal rocks documented in Guyang, Wuchuan, Serteng, and Alxa [60]. The overlap in timing of magmatic activity in the original TTG gneiss and mafic intrusive rocks, combined with Hf isotope characteristics of Neoarchean zircons, suggested that their genesis was related to large-scale mantle magma intrusion [61]. Therefore, the zircon samples we retrieved might have come from the old-aged TTG gneiss and mafic granulite within the Yinshan massif.

Detrital zircons from the Paleoproterozoic (2500–1900 Ma) accounted for ~70% of the measured detrital zircon ages, broadly split into 2500–2300 Ma and 2000–1800 Ma. These ages corresponded well with the Paleoproterozoic (2500–2300 Ma) and with previously calculated ages: $^{207}Pb/^{206}Pb$ surface age of 2510–2350 Ma for zircons originating from granulites of the Guyang Wuchuan area in Inner Mongolia [62], U–Pb age of 2494–2384 Ma for single zircon grains from Yingyun diorite gneiss [63], 2494 ± 59–2371 ± 38 Ma for zircon from potassium granites in the Wulashan Jining area [64], and $^{207}Pb/^{206}Pb$ surface age of 2503–2485 Ma for charnockite zircon in Hadmengou-Pingfanggou area of Daqingshan [65]. Comparative examination of age spectra indicated that the Paleoproterozoic detrital zircon populations investigated here correlate with the widely exposed Precambrian basement lithologies in the Wulashan-Daqingshan structural zone of the NCC's northern margin. These source rocks include Neoarchean granitic gneisses, Paleoproterozoic granulite facies metamorphic rock series, and syn-orogenic granitoid intrusions.

The 2000–1800 Ma age interval corresponds to the ages of metamorphic zircon and highly peraluminous granite occurring in the basin's northern region. For example, the metamorphic age distribution of Khondalites in Daqingshan, Wulashan, and Helanshan ranges from 2.0 to 1.81 Ga [66,67]. Later isomorphic S-type granites are approximately 1.9 Ga old [68]. Liu et al. [69] reported that Daqingshan syenite is approximately 1.82 Ga old, while the systematic petrogeochemical studies of Wang et al. [70] and Xu et al. [71] jointly discovered an A-type granite belt ca. 1.6–1.80 Ga in Daqingshan. We thus speculated that the 2000–1800 Ma detrital zircons in this study originated mainly from granite and Khondalites in Wulashan-Daqingshan. Khondalites from the Bayannula Helan Mountain area (typically 2.6 Ga old) yielded zircons with a two-stage Hf age range of 3159–2074 Ma [66]. Our Hf isotope characteristics indicated that the zircon source area mainly comprises ancient crustal recycled materials, with additional involvement of depleted mantle at 2.0 Ga. The peak ages of the two-stage Hf modes of the three samples in this study are concentrated between 2.71 and 2.27 Ga. Among them, for zircons having ages in the interval of 2.3–1.8 Ga, their two stage Hf model ages cluster between 3373 Ma and 2054 Ma, with an average of 2641 Ma. Their Hf isotope characteristics indicate that there are materials from both crustal and depleted mantle sources.

Magmatic activity during the time interval from the Carboniferous epoch to the Early Permian epoch is linked to the extensional tectonic processes of the Xingmeng orogenic belt that manifested in the early stage of the Late Paleozoic. The Xingmeng orogenic belt, positioned in the central-eastern Inner Mongolia and on the northern edge of North China, contains diverse rock types. Significantly, Late Carboniferous (302–337 Ma) granitic intrusive rocks are distributed in the regions of Sunite Left Banner, Xilinhot, and West Wuzhumuqin Banner [72]. This orogen developed bimodal intrusive and volcanic rocks during the Late Carboniferous Daqingchang period (310–330 Ma). The youngest harmonic age of tuffaceous sandstone and tuff from Erlian and Ailige Temple is 298–302 Ma [73]. Therefore, detrital zircons from 200 to 500 Ma predominantly come from the northern boundary region of the North China Block. It can be inferred that detrital zircons in the Yihewusu Huanhe Formation, dated to the Paleozoic, mainly come from Khondalites in Jining, Daqingshan, Wulashan, Ganlishan, and Helanshan, while a smaller proportion may come from gneiss and granulites in areas such as Guyang or Wuchuan. Building upon previous research [74–80], we compared the zircon U-Pb ages of rocks from the Telaaobao study area with those of other rock masses in the northern Ordos Basin. The comparative age spectra are presented in Figure 11. The zircon age probability density plot (Figure 11) reveals minor detrital zircon populations with crystallization ages clustering at ca. 3.0 Ga in the Langshan-Alxa Eastern Margin tectonic belt. These Neoarchean zircons may constitute secondary provenance contributors to the studied sedimentary succession, potentially deriving from unexposed ancient crustal remnants within the western NCC.

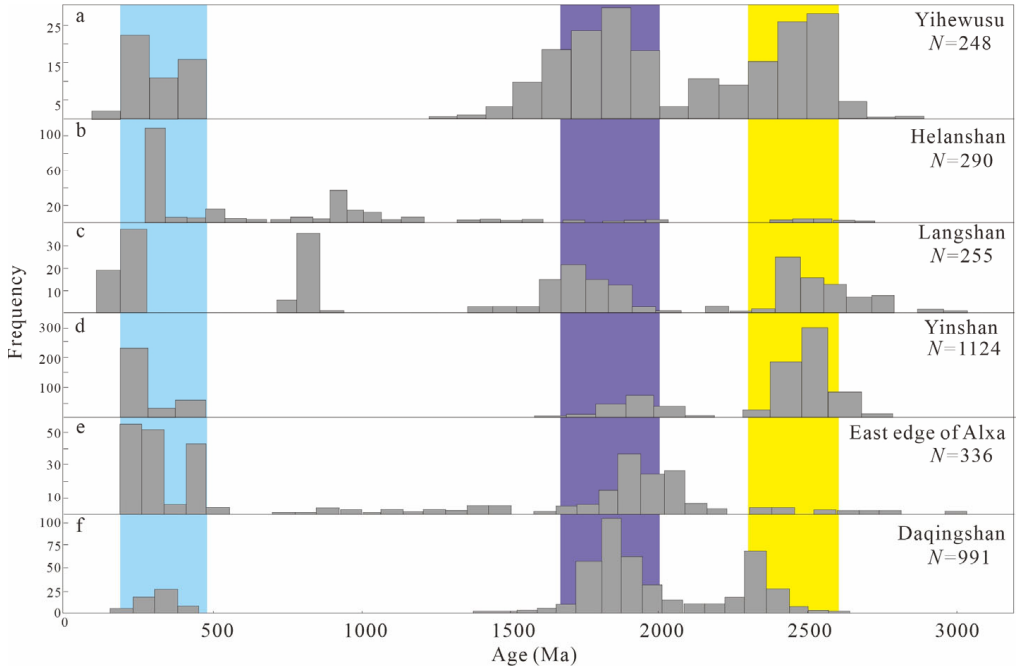

Figure 11. A Comparative Analysis of Zircon U-Pb Age Spectra: Sandstone from the Yihewusu Section of the Huanhe Formation and Adjacent Regions (Revised by previous research [74–80]). Letters a–f denote zircon U-Pb age spectra datasets (a = target horizon in the study area; b–f = adjacent regions). Colors represent three concentrated age intervals: light blue (~200–500 Ma, younger tectonic/magmatic events), dark blue (~1700–2000 Ma, middle-stage crustal evolution), and yellow (~2300–2600 Ma, Archean-Paleoproterozoic crustal formation). *N* indicates the number of valid zircon grains analyzed for U-Pb dating at each location (e.g., *N* = 248 for Yihewusu).

5.2. Geodynamic Setting

The NCC preserves a complex evolutionary sequence characterized by multiple phases of tectonic reactivation. The late Neoarchean (ca. 2600–2300 Ma) represents a pivotal stage in

the craton's tectonic evolution, marked by the formation of large scale volcanic-sedimentary assemblages [81]. This stage includes three main events: formation of Neoarchean greenstone belts, emplacement of crust-derived granitic magmatism controlled by ancient arc-continent collision regimes, and crustal anatexis leading to the accretion of TTG gneisses. Late Neoarchean granitic rocks can be split into groups of 2550–2530 Ma, 2510–2500 Ma, and 2500–2450 Ma, each with distinct lithological associations—high-Na TTG suites, monzogranites, and high-K granites, respectively. Furthermore, early Neoarchean plutons are increasingly found across multiple terranes of the NCC [82]. Zircon isotopic dating from representative regions such as the Yinshan block and Ordos block revealed that these rocks predominantly comprise tonalite, constituting diagnostic TTG suites. These ancient plutons universally experienced overprinting by late Neoarchean (ca. 2500 Ma) tectonothermal events, providing critical evidence for the terminal Neoarchean amalgamation of continental blocks in the NCC. Detrital zircon U-Pb ages of 2600–2300 Ma, as determined from the Huanhe Formation sandstones in this research, exhibit a significant correlation with the magmatic-tectonic evolutionary stages. This correlation strongly indicates that the corresponding interval witnessed intense magmatic events, accompanied by substantial metamorphic and deformational activities.

Zhai and Peng [83] proposed that during the Paleoproterozoic at ca. 1900 Ma, cratonic reactivation of the NCC triggered mantle upwelling events, accompanied by gabbroic magma underplating. These processes induced the development of ultrahigh-temperature metamorphism in regions such as the Daqingshan area, culminating in a regional compressional tectonic event at ca. 1850 Ma. These changes have led to suggestions that the late Paleoproterozoic (ca. 1850 Ma) represents a milestone tectonothermal episode in the NCC's evolutionary history [84]. The Central Orogenic Belt exhibits diagnostic paired metamorphic belts (high-pressure granulite facies and amphibolite facies), foreland thrust-fold systems, and calc-alkaline volcanic-plutonic assemblages with arc affinities. Together with zircon U-Pb isotopic records revealing a continuous age spectrum of 1900–1800 Ma, these features indicated the conclusion of the continent-continent collisional orogenic process among the eastern and western blocks of the North China Craton (NCC) throughout this period. This research revealed that the detrital zircon U-Pb age distributions of the Huanhe Formation sandstones featured a distinct peak around 1850 Ma within the 2000–1700 Ma time range (Figure 9), which implies multiple phases of tectono-magmatic reactivation events during the late Paleoproterozoic era.

The orogenic margins located in the southern and northern parts of the NCC underwent multi-cyclic composite orogenic processes from the Early Paleozoic to the Mesozoic. In particular, the Yinshan intracontinental orogenic belt at the northern margin showed intense tectonic reactivation [85]. The tectonic development of the area was controlled by an entire Wilson Cycle. Initially, the Paleo-Asian oceanic plate continuously subducted beneath the NCC in the Early Paleozoic. Subsequently, an accretionary collision took place in the Late Carboniferous, and the cycle concluded with a continental collision during the Permian. Zircon thermochronological data revealed that the Inner Mongolia Uplift experienced rapid uplift-exhumation processes during 200–300 Ma [86]. Therefore, Zhang et al. [87] hypothesized that for the eastern part of the northern margin of the North China Craton (NCC), the ultimate closure of the Paleo-Asian tectonic realm during the tectonic evolution in the Late Paleozoic-Early Mesozoic era occurred in the early Middle Triassic (ca. 245 Ma). Multidisciplinary evidence indicates that syn-collisional granites yield zircon U-Pb ages clustered at 248–240 Ma. The precisely determined 243 $\pm$ 3 Ma peak metamorphic age of high-pressure rocks like glaucophane-bearing schists, when correlated with other geological information, provides detailed and accurate tectono-thermochronological limitations. The findings collectively confirm a complete disintegration of the Paleo-Asian

tectonic regime, marking its transition into an intracontinental evolutionary stage. Detrital zircons obtained from the Huanhe Formation sandstones in the present research, having ages between 500 and 200 Ma, presumably captured volcanic activities associated with the Inner Mongolia Uplift and enhanced the understanding of the subduction processes of the Paleo-Asian oceanic plate under the North China Block.

Mesozoic sandstone-hosted uranium reservoirs in the Ordos Basin are primarily hosted within multiple stratigraphic units, including the Yan'an Formation, Zhiluo Formation, Luohe Formation, and Huachi Formation. The spatial distribution of these uranium reservoirs and the uranium mineralization processes were significantly influenced by tectonic evolution during different periods. The Late Jurassic to Early Cretaceous represents one of the most critical periods of tectonic activity in the Ordos Basin since the Late Paleozoic. During this interval, the regional tectonic trend ultimately shifted from approximately E-W to nearly N-S or NNE, accompanied by intense magmatic activity [88]. Controlled by a regional compressional stress field, the entire basin underwent rapid subsidence within a depression. Simultaneously, intense tectono-thermal events resulted in the development of a high geothermal field within the basin. This accelerated the thermal maturation process of deep source rocks, driving them into the peak stage of hydrocarbon generation and expulsion, and prompting the large-scale generation and migration/accumulation of natural gas [89]. Since the Late Cretaceous, influenced by the far-field effects of the India-Eurasia plate convergence, the Ordos Basin began to experience overall uplift and denudation. The northern margin of the basin was subjected to intense tectonic compression, leading to the development of large-scale folds and thrust faults [90]. Accompanying the uplift process, a series of minor uplifts developed, forming favorable structural traps and fluid migration pathways. Critically, hydrocarbon reservoirs formed by deep Upper Triassic Yanchang Formation source rocks were affected by fault activity [91]. This triggered the upward migration of deep reducing fluids. The coupling of these reducing fluids with surficial oxygenated, uranium-bearing fluids ultimately initiated the sandstone-hosted uranium mineralization process [92].

5.3. Implications for Initial Uranium Sources

The geochemical composition of sedimentary rocks offers key insights into their source materials and plays a fundamental role in reconstructing the tectonic settings in which they were deposited [93]. Rare earth element (REE) distribution patterns, particularly negative Eu anomalies, are widely used as reliable indicators for determining sedimentary provenance [94]. The North American Shale Composite-normalized REE pattern is nearly flat to slightly right-sloping (Figure 7b), suggesting that the detrital sediments were derived from a continental upper crustal source. The samples exhibit high LREE/HREE ratios (ranging from 4.86 to 36.23) and low Eu/Eu* values (between 0.57 and 2.33) (Appendix A, Table A1), suggesting a felsic origin. Previous studies have indicated that negative Eu anomalies are typically associated with parent rocks such as acidic volcanic rocks and granites [95,96]. Furthermore, felsic rocks are generally characterized by elevated average uranium content, which is consistent with the inferred provenance.

Zircon U-Pb age data indicated a dominant Archean age cluster at approximately 2.5 Ga, correlating with Meso-Neoarchean crustal growth events of the NCC [97]. This suggested that the Archean crust may have served as a primary uranium reservoir, particularly when considered in conjunction with the elevated uranium abundances (3.2–4.8 ppm) within the basement TTG suites. Notably, Hercynian granite (262 Ma) had significantly higher εHf(t) values (range: 1.35–5.62) than Archean zircons, suggesting that their source may have incorporated mantle-derived material [98]. Hercynian granite contained uranium concentrations exceeding crustal averages, with ubiquitous micro-fractures in feldspar

phenocrysts (Figure 6A) providing structural pathways for uranium release. The relatively prominent columns of U (uranium) content for acid intrusive rocks in some periods may imply that they play a specific role in the enrichment of uranium elements (Figure 12). The high feldspar content (15–60%) and abundant Hercynian granitic detritus in northern basin sandstones further substantiate igneous contributions to uranium sources [99].

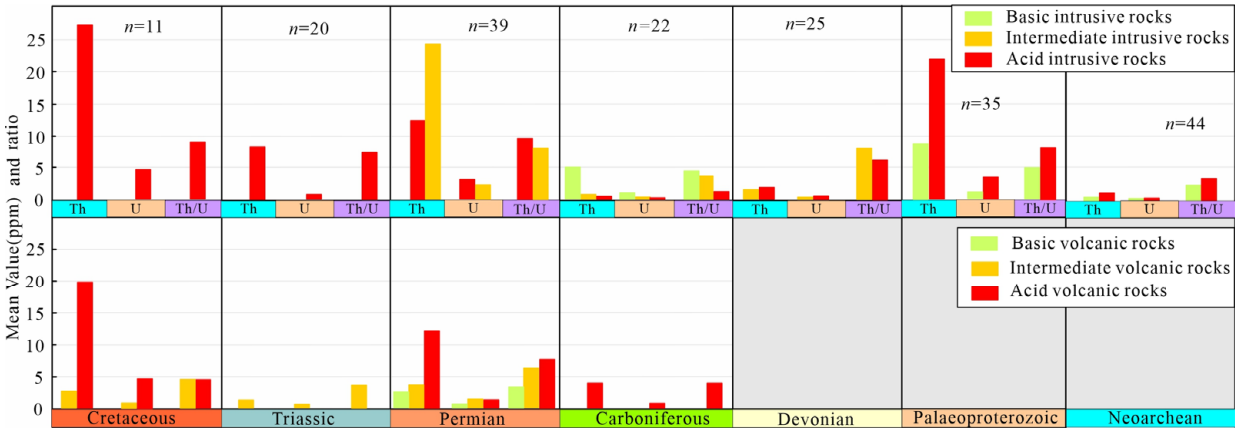

Figure 12. Comparative Assessment of Average U-Th Contents and Th/U Ratios: Intrusive (Upper Graphic) versus Extrusive Volcanic (Lower Graphic) Rocks from the Northern Ordos Basin. (Scale: Y—axis units: Th, U in μg/g; Th/U ratio unitless; *n* = sample number).

In this study, Th and U contents as well as Th/U ratios of the rock masses around the northern Ordos Basin were compiled from the data reported in references [100–107], yielding a comparative diagram of these parameters between intrusive and extrusive rocks (Figure 12). The average Th/U ratio of the Earth's crust is 3 to 4 [108,109]. Consequently, a Th/U ratio exceeding 4 in a rock suggests potential uranium loss, with the released uranium capable of migrating into basins for enrichment and mineralization [110]. In the northern Ordos Basin, intermediate-felsic igneous rocks exhibit a slight enrichment in Th/U ratio compared to ultramafic-mafic compositions (Figure 12). Most of these intermediate-felsic rocks possess Th/U ratios higher than, or significantly higher than 5. The Carboniferous felsic intrusive rocks are an exception, showing a slightly lower average Th/U ratio of 3.5, indicating they underwent minor uranium loss. Therefore, the uranium sources in the study area comprise two components: (1) Permian-Cretaceous intermediate-felsic rocks likely released mobilized uranium contributing to enrichment and mineralization, and (2) Neoarchean-Carboniferous intermediate-felsic rocks primarily supplied uranium-bearing clastics to the basin, although the amount of uranium exported from these older source rocks was generally limited.

Our inference that Devonian-Cretaceous intermediate-felsic igneous rocks along the northern margin of the Western North China Craton served as the principal uranium reservoirs aligns with models from Songliao and Yili basin. In the Songliao basin, widespread felsic volcanism and thick tuffaceous inputs supplied U-bearing detritus and leachable glass/feldspar [111–113]; meteoric oxidation followed by hydrocarbon-sulfur reductants focused U fixation in feldspathic-lithic reservoirs near facies transitions [114]. In the Yili basin, uplift of the Tianshan delivered proximal U-bearing intermediate-felsic detritus [115]; high-relief catchments and pervasive feldspar micro-fracturing enhanced U mobilization and transport to roll-front redox traps [116,117]. Shared features—magmatic sources showing U loss (elevated Th/U), labile feldspar-lithic grains that intensify fluid-rock interaction, and proximal fluvial-lacustrine traps—mirror the Huanhe Formation, reinforcing a regional source–transport–trap framework. A key contrast is the dominance of syn-depositional volcanic supply in Songliao versus basement-derived, proximally recycled

detritus in Yili and this study, guiding screening of felsic source belts, tuffs, and feldspar micro-fracture intensity.

6. Conclusions

1. The U-Pb ages of detrital zircons within Huanhe Formation sandstones can be categorized into three distinct age groups: Phanerozoic (500–200 Ma), Paleoproterozoic (2000–1700 Ma), and Neoarchean (2600–2300 Ma); the three age groups correspond to the subduction of the Paleo-Asian Ocean plate beneath the northern margin of the North China Craton and the closure of the Paleo-Asian Ocean during the Ordovician to Triassic periods, the multiple phases of tectono-magmatic reactivation events in the late Paleoproterozoic, and the stage of initial continental nucleus formation during the Neoarchean to Paleoproterozoic.

2. Shifts in the relative proportions of zircon age populations reveal significant changes in sediment provenance from the Neoarchean to the Mesozoic. The Yinshan Block and Central Orogenic Belt of the North China Craton (NCC)—composed predominantly of TTG gneisses, granulites, and khondalites—likely represent the primary source regions for detrital zircons in these sandstones. Additionally, Phanerozoic igneous rocks contributed distinct pulses of zircon ages (500–200 Ma) to contemporaneous strata during the Late Jurassic to Cretaceous.

3. Relative to the older Neoarchean-Carboniferous igneous suite, the Devonian-Cretaceous intermediate-felsic rocks along the northern margin of the Western North China Craton have source-favorable attributes (higher bulk U contents, more samples with elevated Th/U ratios >5, and pervasive feldspar micro-fracturing). These characteristics confirm them as the dominant uranium reservoirs and primary sources of mobilized/fluid-transported U and U-enriched detrital components for the ore-hosting Huanhe Formation in the northern Ordos Basin. This finding explicitly identifies it as a key target for future uranium prospecting in the region and provides a geological basis for narrowing down high-potential exploration areas of Huanhe Formation-hosted uranium deposits.

Author Contributions: Conceptualization, X.Z. and F.N.; methodology, C.Z.; software, J.C.; validation, X.Z., Z.Y.; formal analysis, J.C. and Z.Y.; investigation, X.Z. and J.C.; resources, F.N.; data curation, X.Z. and Y.H.; writing—original draft preparation, X.Z. and J.C.; writing—review and editing, X.Z. and J.C.; visualization, J.C.; supervision, F.N.; project administration, A.M.; funding acquisition, F.N. All authors have read and agreed to the published version of the manuscript.

Funding: This article is jointly supported by the National Natural Science Foundation of China (U2244205; 42272097), the Foundation of National Key Laboratory of Uranium Resources Exploration-Mining and Nuclear Remote Sensing (2024HDX05; 2025QZ-YZZ-08; NKLUR-WDZC-2025-01), as well as the Science and Technology Plan Project of Jiangxi Provincial Department of Education (GJJ2400612).

Data Availability Statement: All data generated or analyzed during this study are included in this article.

Acknowledgments: We sincerely thank the Nuclear Resources and Environment team at East University of Technology for advising and assisting with experimental analyses. We also gratitude anonymous reviewers and editors for their insightful comments.

Conflicts of Interest: Authors Aisheng Miao and Yujie Hu was employed by the company Nuclear Industry Co Ltd. The remaining authors declare that the research was conducted in the absence of any commercial or financial relationships that could be construed as a potential conflict of interest.

Appendix A

Table A1. The REE contents (10^{-6}) of the sandstone sample from the Huanhe Formation.

	ER1	ER2	ER3	ER4	ER5	ER6	ER7	ER8	ER9	ER10
La	58.90	158.70	144.80	41.60	16.60	9.20	391.00	34.20	161.80	59.20
Ce	103.20	301.00	282.80	77.80	27.40	19.80	712.80	62.50	288.40	98.60
Pr	10.40	32.70	31.80	6.80	3.24	3.04	62.98	6.58	30.60	11.20
Nd	36.00	122.10	111.90	21.40	12.00	13.10	192.80	22.60	121.80	35.80
Sm	5.92	16.90	15.10	2.71	2.11	2.94	20.60	3.54	17.10	6.10
Eu	2.36	2.21	2.77	0.91	1.04	1.04	3.75	0.63	2.18	2.27
Gd	6.52	16.10	13.50	2.94	1.83	2.46	26.30	3.35	16.30	12.40
Tb	1.12	2.11	1.37	0.35	0.31	0.50	2.47	0.50	2.27	1.21
Dy	4.97	7.21	2.84	1.13	1.36	2.55	5.81	2.08	7.36	4.97
Ho	0.93	1.18	0.24	0.18	0.26	0.54	0.59	0.37	1.24	0.94
Er	2.81	4.16	0.72	0.70	0.83	1.65	1.64	1.13	4.24	2.74
Tm	0.42	0.46	0.06	0.09	0.12	0.27	0.15	0.17	0.45	0.19
Yb	3.04	3.16	0.51	0.60	0.84	1.88	1.11	1.14	3.15	2.84
Lu	0.45	0.46	0.07	0.09	0.11	0.26	0.13	0.17	0.47	0.25
Y	25.80	27.60	5.33	5.24	7.48	15.40	18.80	10.50	27.40	25.60
Th	1.84	8.62	29.95	15.86	4.65	0.66	128.96	23.70	8.76	1.82
U	2.92	12.37	3.21	0.84	1.27	1.33	5.86	11.40	12.47	2.88
Eu/Eu*	1.66	0.59	0.86	1.40	2.33	1.70	0.71	0.81	0.57	1.15
LREE	216.78	633.61	589.17	151.22	62.39	49.12	1383.93	130.05	621.88	213.17
HREE	20.26	34.84	19.31	6.08	5.66	10.11	38.2	8.91	35.48	25.54
LREE/HREE	10.70	18.19	30.51	24.87	11.02	4.86	36.23	14.60	17.53	8.35
ΣREE	237.04	668.45	608.48	157.30	68.05	59.23	1422.13	138.96	657.36	238.71

Eu* represents the chondrite-normalized theoretical calculated value of europium.

Table A2. LA-ICP-MS U-Pb dating data from Huanhe formation in the northwestern Ordos Basin.

Spot. No	Th	U	Th/U	$^{207}Pb/^{206}Pb$	2s(abs)	$^{207}Pb/^{235}U$	2s(abs)	$^{206}Pb/^{238}U$	2s(abs)	(Concordant) %
ER21-02	50	72	0.69	1476	201.08	1574	82.65	1633	80.41	96.30
ER21-03	108	216	0.50	2553	70.16	2479	37.75	2364	56.01	95.30
ER21-05	44	55	0.80	1538	249.76	1470	89.88	1377	85.58	93.50
ER21-06	138	461	0.30	2372	59.15	2174	32.60	1957	44.26	89.50
ER21-07	104	208	0.50	2492	70.33	2394	40.15	2288	66.94	95.50
ER21-08	670	1340	0.50	307	194.98	309	18.99	297	10.08	95.90
ER21-09	410	513	0.80	2548	46.27	2553	23.62	2554	59.52	99.90
ER21-12	226	226	1.00	2477	73.50	2393	41.06	2319	64.55	96.90
ER21-14	182	260	0.70	1923	109.61	1853	51.87	1788	59.69	96.40
ER21-16	153	153	1.00	2459	86.10	2357	47.63	2254	69.83	95.50
ER21-19	68	338	0.20	1952	88.19	1891	43.16	1822	58.08	96.30
ER21-26	167	239	0.80	1758	94.74	1647	46.58	1528	40.09	92.50
ER21-28	28	31	0.90	1252	397.89	1567	121.34	1676	134.15	93.30
ER21-31	213	266	0.70	2275	72.45	2220	38.19	2086	57.31	93.80
ER21-32	706	784	0.60	22	241.39	260	24.26	273	10.11	95.40
ER21-33	223	319	2.10	2430	68.17	2362	35.97	2201	55.73	93.00
ER21-34	110	183	0.90	470	424.04	311	52.46	248	16.98	89.60
ER21-35	86	41	1.10	2390	158.91	2313	86.34	2139	104.93	92.20
ER21-36	360	400	2.61	2361	55.10	2442	32.90	2464	64.59	99.10
ER21-38	229	208	0.80	1284	164.88	1247	60.09	1191	51.84	95.40
ER21-39	47	18	0.80	2483	212.68	2509	124.08	2474	190.45	98.60
ER21-40	83	104	1.10	1963	191.11	1866	91.05	1724	75.88	92.10
ER21-41	185	231	1.00	1619	70.56	1665	36.32	1603	65.70	98.40
ER21-42	376	342	0.50	2385	61.40	2405	34.55	2355	48.61	97.90
ER21-43	510	510	0.90	548	192.22	476	34.03	436	16.94	91.20
ER21-44	217	433	1.30	2411	59.29	2401	30.54	2326	51.77	96.90
ER21-45	360	400	0.80	2361	55.10	2442	32.90	2464	64.59	99.10
ER21-47	99	76	0.60	1734	117.47	1782	54.94	1794	96.47	96.20
ER21-49	185	231	0.80	2359	70.56	2465	36.32	2503	65.70	98.40
ER21-50	264	440	0.30	582	249.42	464	37.12	419	19.46	89.70
ER21-52	58	191	0.20	1682	117.12	2336	54.21	2198	46.92	96.50
ER21-53	80	800	0.50	346	148.85	288	17.23	261	7.09	90.40
ER21-54	65	323	4.00	2277	83.85	2142	46.47	2028	47.55	94.50
ER21-55	63	126	0.59	1976	110.37	1914	51.21	1854	65.12	96.80
ER21-56	512	128	0.00	1785	75.31	1878	34.52	1964	41.69	95.90
ER21-57	20	34	0.69	1728	272.03	1793	102.44	1790	106.90	99.80
ER21-59	37	261	0.14	1746	141.71	1701	101.34	1665	111.73	96.60
ER21-60	71	353	0.20	2033	82.98	1986	34.46	1949	48.87	98.10
ER21-61	196	115	1.70	1828	77.02	1703	50.11	1604	63.84	92.90
ER21-62	61	66	0.92	1916	123.53	1862	96.14	1813	107.77	94.00
ER21-63	52	86	0.60	1670	166.81	1709	66.56	1704	79.51	99.70
ER21-64	523	564	0.93	1807	50.13	1770	32.11	1748	46.45	93.90
ER21-65	69	677	0.10	1822	55.61	1745	21.04	1640	28.26	94.70
ER21-67	24	119	0.10	1963	191.11	1845	91.05	1864	75.88	99.00
ER21-68	881	729	1.20	1848	56.81	1905	23.56	1853	34.04	96.60
ER21-69	37	62	1.20	1863	257.68	1725	105.90	1573	76.37	94.00
ER21-70	169	228	0.81	1754	93.56	1643	47.26	1529	41.03	90.60
ER21-71	121	108	1.12	1970	96.29	1944	47.15	1914	34.02	98.00
ER21-72	226	496	0.45	2165	79.63	2121	42.27	2067	37.10	97.00
ER21-73	44	255	0.17	1876	87.04	1638	40.50	1452	33.93	87.00
ER21-74	285	1325	0.22	2384	69.44	2539	40.33	2726	49.47	92.00

Table A2. *Cont.*

Spot. No	Th	U	Th/U	$^{207}Pb/^{206}Pb$	2s(abs)	$^{207}Pb/^{235}U$	2s(abs)	$^{206}Pb/^{238}U$	2s(abs)	(Concordant) %
ER21-75	130	172	0.76	76	211.08	256	21.55	276	7.72	92.00
ER21-76	85	142	0.60	1567	83.33	1658	36.43	1733	31.00	95.00
ER21-77	439	392	1.12	502	188.87	334	24.02	311	7.96	92.00
ER21-78	305	182	1.68	2325	62.50	2344	35.00	2357	39.55	99.00
ER21-79	13	33	0.40	1576	131.48	1596	56.61	1619	44.11	98.00
ER21-80	198	746	0.27	1789	64.82	1765	31.14	1738	29.88	98.00
ER21-81	60	108	0.56	2605	68.21	2655	42.35	2710	51.39	97.00
ER21-82	54	135	0.40	2361	63.74	2326	39.00	2281	43.25	98.00
ER21-83	281	438	0.64	254	168.50	275	17.35	278	6.62	98.00
ER21-84	32	76	0.42	2602	79.48	2577	59.95	2529	90.21	98.00
ER21-85	146	192	0.76	143	224.04	267	21.70	283	7.22	94.00
ER21-86	57	107	0.53	332	340.70	179	22.74	158	6.20	87.00
ER21-87	98	153	0.64	300	201.83	271	21.34	267	7.74	98.00
ER21-88	104	210	0.50	1692	69.91	1705	31.44	1708	27.30	99.00
ER21-89	72	186	0.39	2409	60.18	2260	33.68	2091	34.86	92.00
ER21-90	26	129	0.20	2087	77.93	2068	52.73	2025	54.44	97.00
ER21-91	55	104	0.53	2318	69.60	2351	38.58	2379	44.51	98.00
ER21-92	371	510	0.73	287	153.69	290	17.52	289	7.34	99.00
ER21-93	168	224	0.75	2343	68.06	2281	36.72	2207	42.19	96.00
ER21-94	79	116	0.68	1603	101.39	1614	43.84	1618	29.44	99.00
ER21-95	51	34	1.53	2139	118.37	2125	77.53	2074	76.42	97.00
ER21-96	235	218	1.08	1676	89.19	1481	41.15	1342	35.25	90.00
ER21-97	33	45	0.73	1635	116.36	1632	48.11	1637	43.37	99.00
ER21-98	62	115	0.54	550	198.12	438	30.80	420	11.30	95.00
ER21-99	70	160	0.44	309	248.12	262	24.05	255	6.90	97.00
ER21-100	95	131	0.72	2500	70.37	2472	39.96	2442	43.42	98.00
ER21-101	17	50	0.33	2607	87.35	2610	52.20	2608	59.84	99.00
ER21-102	16	48	0.34	478	383.29	364	44.96	298	13.27	80.00
ER21-103	69	114	0.61	2592	88.89	2578	50.89	2559	63.30	99.00
ER25-01	59	591	1.70	1701	85.91	1542	33.56	1394	40.94	90.00
ER25-02	534	314	0.80	1924	76.68	1870	34.58	1781	46.28	95.10
ER25-05	118	148	0.40	2439	76.95	2450	33.46	2438	81.92	99.50
ER25-06	177	443	1.60	1719	79.13	1694	40.86	1634	51.05	96.40
ER25-07	48	30	0.90	2492	173.42	2402	98.33	2300	146.76	95.70
ER25-08	192	213	0.10	2119	85.73	2083	49.84	2000	64.37	95.90
ER25-09	25	245	1.20	2457	72.61	2447	37.30	2382	65.16	97.30
ER25-10	65	54	0.60	2402	136.01	2295	70.95	2124	101.55	92.30
ER25-11	75	125	0.60	1676	156.13	1660	61.61	1587	65.33	95.50
ER25-12	268	447	1.00	243	277.28	314	30.48	304	10.43	97.00
ER25-13	169	169	0.20	1822	112.13	1801	51.06	1724	56.15	95.70
ER25-14	36	181	0.50	1685	118.05	1761	53.77	1774	46.95	99.20
ER25-15	153	306	0.70	2378	54.01	2344	33.54	2252	59.64	96.00
ER25-16	227	324	0.50	51	336.09	267	34.81	287	17.00	92.80
ER25-17	215	429	1.40	1858	69.24	1876	33.70	1825	55.39	97.20
ER25-18	749	535	0.30	366	279.15	307	31.63	288	12.05	93.50
ER25-20	129	430	0.50	377	225.41	450	34.73	421	16.10	93.40
ER25-23	75	141	0.40	1881	87.90	1828	52.18	1781	50.35	92.60
ER25-24	353	891	0.90	1835	43.35	1770	25.30	1715	49.69	98.80
ER25-26	382	424	0.60	631	244.22	488	48.56	443	17.15	90.40
ER25-27	526	876	0.60	2174	44.54	2228	22.74	2191	46.87	98.40
ER25-28	385	642	1.00	375	180.75	437	26.62	426	14.13	97.60
ER25-29	455	455	0.80	2442	39.01	2416	32.88	2317	52.60	95.80
ER25-30	148	185	0.70	2386	76.88	2400	44.20	2324	65.38	96.80
ER25-31	77	110	0.30	1990	115.89	1878	56.15	1718	64.67	91.10
ER25-32	268	892	0.70	1851	51.81	1878	25.30	1833	39.98	97.60
ER25-33	165	236	0.60	1871	74.54	1878	38.54	1888	64.68	95.80
ER25-34	393	655	1.10	317	330.92	324	33.78	315	13.22	97.10
ER25-35	446	405	0.40	2474	46.41	2473	26.33	2410	42.90	97.40
ER25-38	303	758	0.60	2002	57.08	1895	25.56	1780	39.46	93.70
ER25-39	38	63	1.20	1867	258.12	1727	106.20	1562	76.65	90.00
ER25-40	133	111	1.00	2175	109.10	2164	63.03	2149	107.40	99.30
ER25-41	802	802	0.80	2253	45.00	2250	29.39	2229	46.93	99.00
ER25-43	130	162	0.14	2359	86.57	2217	50.62	2075	96.23	93.40
ER25-46	228	285	0.80	2500	58.88	2427	38.72	2325	59.23	95.70
ER25-47	163	233	0.70	670	458.01	305	54.07	271	22.10	88.20
ER25-49	73	734	0.10	435	185.86	418	30.30	397	14.44	94.80
ER25-50	53	178	0.30	2360	84.66	2270	41.11	2153	65.59	94.70
ER25-51	204	681	0.30	437	220.31	449	33.94	424	16.12	94.30
ER25-52	76	189	0.40	435	185.86	2368	30.30	2298	14.44	94.50
ER25-53	181	439	1.59	1711	78.95	1692	40.14	1614	51.14	94.40
ER25-54	750	536	1.40	243	277.28	307	30.48	302	10.43	93.60
ER25-55	128	425	0.30	377	225.41	450	34.73	421	16.10	93.40
ER25-57	171	171	1.00	2303	98.35	2336	50.22	2246	77.80	96.10
ER25-58	37	179	0.14	1822	113.11	1803	51.61	1725	55.93	94.80
ER25-59	150	299	0.50	1870	58.88	1792	38.75	1725	59.55	95.70
ER25-60	152	190	0.80	1869	76.68	1878	44.24	1887	64.50	96.80
ER25-61	75	107	0.70	1791	114. 54	1747	56.16	1739	64.63	91.10
ER25-62	146	112	1.30	1836	106.60	1821	63.14	1600	69.50	99.30
ER25-64	54	181	0.30	1681	117.12	2336	54.20	2198	46.95	96.00
ER25-65	209	697	0.30	435	185.86	432	30.30	397	14.44	94.80
ER25-68	383	425	0.90	367	376.65	491	34.73	421	16.10	93.40
ER25-70	383	425	0.90	1867	248.16	1887	107.47	1848	76.65	92.50
ER25-71	62	112	0.55	2506	103.86	2471	56.84	2428	59.03	98.00
ER25-72	36	47	0.77	191	370.33	334	32.86	287	13.76	84.00

Table A2. *Cont.*

Spot. No	Th	U	Th/U	$^{207}Pb/^{206}Pb$	2s(abs)	$^{207}Pb/^{235}U$	2s(abs)	$^{206}Pb/^{238}U$	2s(abs)	(Concordant) %
ER25-73	15	22	0.68	1765	212.04	1696	92.96	1670	74.98	98.00
ER25-74	57	181	0.31	1911	101.85	1942	47.85	1974	48.23	98.00
ER25-75	120	211	0.57	2435	87.04	2397	48.70	2354	65.46	98.00
ER25-76	38	83	0.46	2500	89.20	2468	48.14	2444	58.76	99.00
ER25-77	52	89	0.58	1933	95.84	1905	47.58	1937	50.00	98.00
ER25-78	47	103	0.46	2622	78.24	2393	47.19	2134	63.00	88.00
ER25-79	197	208	0.95	295	212.01	319	24.38	324	10.97	98.00
ER25-80	69	89	0.78	2425	75.62	2444	43.63	2463	59.40	99.00
ER25-81	90	428	0.21	2574	71.92	2571	42.21	2562	56.33	99.00
ER25-82	104	678	0.15	2366	72.84	2319	40.85	2261	51.22	97.00
ER25-83	85	289	0.29	1820	77.47	1736	36.78	1661	26.30	95.00
ER25-84	225	682	0.33	257	157.39	288	17.89	291	9.84	98.00
ER25-85	67	92	0.73	2429	79.94	2372	43.81	2297	41.74	96.00
ER25-86	63	113	0.56	1744	101.70	1279	54.79	1012	47.32	76.00
ER25-87	8	27	0.30	2498	88.12	2497	51.51	2494	62.31	99.00
ER25-88	88	102	0.86	2600	73.30	2450	37.72	2345	40.80	95.00
ER25-89	80	82	0.98	2129	83.80	2094	41.07	2059	38.71	98.00
ER25-90	89	136	0.65	2516	64.51	2506	37.06	2484	38.75	99.00
ER25-91	85	157	0.54	2406	69.75	2410	39.71	2413	45.77	99.00
ER25-92	142	178	0.80	2494	67.90	2490	39.64	2480	45.24	99.00
ER25-93	84	89	0.94	1265	101.85	1331	42.05	1367	29.94	97.00
ER25-94	59	303	0.20	1869	75.31	1791	37.12	1719	32.66	95.00
ER25-95	277	404	0.69	302	166.65	280	17.47	277	6.19	99.00
ER25-96	629	736	0.85	2173	64.20	2171	40.03	2157	45.31	99.00
ER25-97	52	68	0.76	1717	94.45	1712	46.03	1699	34.75	99.00
ER25-98	143	150	0.95	1725	75.93	1733	34.13	1733	30.05	99.00
ER25-99	143	149	0.96	457	168.50	438	27.25	432	10.46	98.00
ER25-100	56	117	0.48	600	221.27	457	33.82	440	11.91	96.00
ER25-101	67	282	0.24	1791	72.23	1771	33.45	1745	30.19	98.00
ER25-102	47	76	0.62	2346	83.79	2375	44.32	2393	47.43	99.00
ER25-103	24	24	1.00	2442	108.94	2479	58.82	2519	59.59	98.00
ER25-104	192	218	0.88	261	185.16	289	20.11	293	7.55	98.00
ER25-105	53	310	0.17	2357	79.47	2278	42.74	2173	41.15	95.00
ER25-106	26	271	0.10	1943	79.32	1904	38.46	1855	35.75	97.00
ER25-107	11	22	0.50	500	475.89	433	52.31	286	16.51	58.00
ER25-108	141	181	0.78	2480	66.67	2479	36.43	2463	43.00	99.00
ER25-109	38	55	0.69	1666	115.59	1629	50.46	1596	37.38	97.00
ER50-01	16	27	0.59	1529	295.85	1586	110.95	1601	107.78	97.40
ER50-02	119	199	0.60	2141	61.81	2095	33.02	1994	49.33	95.10
ER50-03	67	673	0.10	1825	56.62	1746	20.73	1639	29.23	93.70
ER50-04	644	1287	0.50	1843	42.95	1835	22.18	1795	33.13	97.80
ER50-05	42	35	1.20	2413	130.40	2220	61.13	1966	103.33	87.80
ER50-06	143	478	0.30	1946	52.18	1956	27.44	1936	42.79	99.00
ER50-07	86	286	0.30	2408	52.06	2341	33.13	2223	43.57	94.80
ER50-08	20	98	0.20	2492	83.95	2386	42.60	2227	63.80	93.20
ER50-11	28	93	0.30	2236	127.42	2063	68.99	1896	73.75	91.50
ER50-14	34	114	0.30	1942	127.10	1989	53.63	2002	56.76	99.40
ER50-15	23	38	0.61	1536	211.46	1546	77.38	1513	72.73	97.80
ER50-16	95	473	0.20	2313	56.03	2222	39.36	2088	44.47	93.80
ER50-21	121	151	0.80	2541	64.46	2512	39.24	2413	61.75	96.00
ER50-23	237	263	0.90	2108	73.82	2056	35.27	1925	48.43	93.40
ER50-26	195	195	1.00	165	427.40	461	62.93	443	19.06	95.90
ER50-28	319	456	0.70	2363	48.46	2246	52.19	2024	96.95	89.60
ER50-30	300	214	1.40	252	265.67	441	42.45	464	23.63	94.90
ER50-32	877	731	1.20	1850	57.79	1909	23.57	1851	34.04	96.90
ER50-33	183	261	0.70	2438	64.78	2382	32.27	2180	46.62	91.10
ER50-35	89	223	0.40	2255	115.03	2334	68.85	2313	74.17	99.10
ER50-36	121	121	1.00	2430	78.82	2498	35.26	2432	72.10	97.30
ER50-38	240	480	0.50	2439	48.38	2399	27.01	2253	46.40	93.70
ER50-39	340	567	0.60	2148	64.83	2009	25.01	1799	40.52	89.00
ER50-45	180	257	0.70	105	368.35	278	37.47	277	16.01	99.50
ER50-47	140	280	0.20	1927	94.63	1954	40.42	1965	47.91	99.40
ER50-48	61	307	0.90	1841	86.25	1620	38.78	1435	42.02	87.90
ER50-49	176	195	1.10	2416	93.77	2391	41.14	2334	64.03	97.60
ER50-52	149	135	2.30	1717	74.19	1713	47.41	1707	71.92	97.30
ER50-53	163	71	0.50	1831	112.33	1766	54.67	1714	99.30	98.10
ER50-55	728	1456	0.10	343	187.45	283	21.59	271	8.76	95.60
ER50-57	79	789	0.71	2402	31.53	2459	18.81	2534	45.12	97.00
ER50-58	17	24	0.10	2374	99.77	2405	53.69	2432	90.67	98.90
ER50-59	14	137	0.40	1848	95.19	1894	61.02	1937	66.13	97.80
ER50-60	51	127	0.20	1785	75.25	1878	34.71	1964	41.88	95.50
ER50-61	8	40	0.60	2380	101.54	2388	57.73	2403	85.25	95.50
ER50-62	89	149	0.60	1793	74.62	1779	59.06	1779	83.50	99.40
ER50-63	98	163	1.00	69	310.49	253	25.72	263	13.49	99.90
ER50-64	63	63	0.50	1877	82.46	1887	52.84	1899	78.50	96.40
ER50-65	63	125	1.00	1787	60.06	1735	28.84	1618	57.94	96.10
ER50-66	145	145	0.40	1948	74.81	1927	32.69	1910	45.53	96.30
ER50-67	55	138	0.51	147	315.09	283	33.56	276	15.14	97.20
ER50-68	20	39	1.53	1739	121.95	1648	64.21	1580	113.16	96.00
ER50-69	23	15	0.30	1738	157.38	1652	80.07	1565	120.47	98.90
ER50-70	50	168	0.80	1523	107.68	1306	56.72	1159	67.09	88.00
ER50-71	53	66	0.20	2001	111.82	1851	54.66	1691	57.24	91.00
ER50-72	52	262	0.50	292	223.12	325	27.52	312	12.07	95.90
ER50-73	36	72	0.40	1692	141.97	1766	63.50	1766	55.91	99.80
ER50-74	42	105	0.60	1656	121.23	1552	64.01	1427	68.10	91.60

Table A2. *Cont.*

Spot. No	Th	U	Th/U	$^{207}Pb/^{206}Pb$	2s(abs)	$^{207}Pb/^{235}U$	2s(abs)	$^{206}Pb/^{238}U$	2s(abs)	(Concordant) %
ER50-75	80	134	0.60	1318	141.94	1376	98.22	1398	120.28	98.40
ER50-76	92	153	0.10	1894	62.61	1782	31.03	1691	52.26	96.20
ER50-77	23	230	0.70	1761	72.44	1584	32.55	1441	38.63	90.50
ER50-78	65	93	0.60	1871	71.46	1792	46.69	1725	64.04	96.40
ER50-80	61	101	0.80	1872	69.40	1858	42.42	1846	65.09	98.00
ER50-83	123	154	0.80	1880	88.33	1827	52.18	1783	60.88	92.60
ER50-84	30	45	0.67	2614	83.95	2555	58.52	2458	54.37	96.00
ER50-85	9	12	0.75	1857	200.46	1769	86.56	1694	58.17	95.00
ER50-86	214	378	0.57	302	216.64	159	13.71	149	3.88	93.00
ER50-87	32	64	0.50	2536	78.40	2473	42.92	2386	48.73	96.00
ER50-88	105	208	0.50	2155	77.78	2141	38.52	2114	36.80	98.00
ER50-89	50	98	0.51	2592	70.22	2492	41.43	2366	45.59	94.00
ER50-90	175	192	0.91	2549	93.06	2561	51.32	2563	51.20	99.00
ER50-91	374	340	1.10	2477	70.68	2483	37.53	2474	34.92	99.00
ER50-92	65	90	0.72	1618	105.56	1651	44.48	1672	33.52	98.00
ER50-93	88	70	1.26	2473	77.93	2486	42.86	2485	44.26	99.00
ER50-94	22	26	0.85	1569	140.74	1644	61.57	1699	49.68	96.00
ER50-95	150	155	0.97	280	233.31	317	27.64	320	7.18	98.00
ER50-96	37	81	0.46	2381	73.92	2384	41.70	2369	39.01	99.00
ER50-97	41	45	0.91	2491	83.80	2482	46.90	2457	49.51	98.00
ER50-98	142	156	0.91	439	202.75	445	30.41	440	10.00	98.00
ER50-99	32	123	0.26	1777	98.61	1612	47.33	1475	36.55	91.00
ER50-100	40	195	0.21	1969	80.24	1963	40.38	1950	38.53	99.00
ER50-101	32	21	1.52	2500	108.49	2489	56.30	2485	65.18	99.00
ER50-102	176	207	0.85	594	168.50	473	26.37	451	12.01	95.00
ER50-103	510	384	1.33	300	166.65	291	17.84	289	6.36	99.00
ER50-104	42	57	0.74	2147	93.21	2118	48.39	2075	45.96	97.00
ER50-105	44	28	1.57	2465	102.78	2437	54.08	2397	51.66	98.00
ER50-106	121	187	0.65	2533	65.90	2559	35.83	2576	41.39	99.00
ER50-107	197	549	0.36	1813	72.38	1562	33.85	1376	33.63	87.00
ER50-108	51	90	0.57	457	374.03	329	34.87	285	10.28	85.00
ER50-109	33	53	0.62	1628	125.92	1539	54.12	1473	37.45	95.00
ER50-110	44	126	0.35	1984	83.79	2001	41.58	2008	41.27	99.00

Table A3. Lu-Hf data of detrital zircons in the Yihewusu area.

Spot. No	$^{176}Hf/^{177}Hf$	1σ	$^{176}Lu/^{177}Hf$	1σ	$^{176}Yb/^{177}Hf$	1σ	Age (Ma)	εHf(t)	t_{DM1}	t_{DM2}
ER21-02	0.281783	0.000013	0.0003	0.000001	0.0110	0.000067	1476	−2.48	2021	2605
ER21-03	0.281721	0.000017	0.0014	0.000021	0.0558	0.000493	1538	−4.39	2164	2799
ER21-05	0.281603	0.000013	0.0005	0.000006	0.0181	0.000289	1538	−7.63	2273	3054
ER21-06	0.281236	0.000015	0.0008	0.000020	0.0335	0.000391	2372	−2.53	2795	3236
ER21-07	0.281316	0.000011	0.0007	0.000004	0.0270	0.000259	2492	3.29	2676	2868
ER21-08	0.282410	0.000013	0.0012	0.000023	0.0385	0.000598	279	−6.89	1194	2130
ER21-09	0.281268	0.000012	0.0006	0.000009	0.0232	0.000260	2548	3.03	2733	2928
ER21-12	0.281195	0.000011	0.0005	0.000006	0.0184	0.000316	2477	−1.03	2825	3193
ER21-14	0.281668	0.000012	0.0004	0.000005	0.0146	0.000263	1922	3.38	2181	2457
ER21-16	0.281292	0.000013	0.0003	0.000008	0.0115	0.000226	2459	2.29	2683	2923
ER21-19	0.281376	0.000012	0.0004	0.000007	0.0153	0.000180	1952	−6.37	2577	3241
ER21-26	0.281559	0.000011	0.0004	0.000004	0.0157	0.000290	1758	−4.18	2328	2936
ER21-28	0.281878	0.000016	0.0005	0.000026	0.0222	0.001023	1252	−4.32	1905	2595
ER21-31	0.281396	0.000011	0.0008	0.000015	0.0287	0.000264	2275	1.02	2577	2891
ER21-32	0.282622	0.000014	0.0007	0.000010	0.0287	0.000268	260	0.27	884	1539
ER21-33	0.281374	0.000013	0.0007	0.000006	0.0273	0.000377	2430	3.96	2597	2772
ER21-34	0.282377	0.000011	0.0009	0.000035	0.0384	0.001564	280	−8.00	1231	2219
ER21-35	0.281299	0.000012	0.0011	0.000012	0.0390	0.000331	2390	−0.26	2726	3072
ER21-36	0.281308	0.000012	0.0012	0.000034	0.0441	0.000901	2361	−0.71	2719	3087
ER21-38	0.282090	0.000012	0.0009	0.000008	0.0369	0.000477	1284	3.59	1631	1990
ER21-39	0.281297	0.000014	0.0003	0.000012	0.0101	0.000362	2483	3.09	2673	2877
ER21-40	0.281351	0.000014	0.0009	0.000077	0.0432	0.005365	1963	−7.70	2645	3352
ER21-41	0.281290	0.000013	0.0004	0.000000	0.0169	0.000123	2359	−0.21	2692	3046
ER21-43	0.282257	0.000011	0.0010	0.000018	0.0399	0.001222	476	−8.06	1401	2358
ER21-45	0.281322	0.000012	0.0003	0.000001	0.0124	0.000080	2361	1.13	2642	2943
ER21-49	0.281321	0.000011	0.0004	0.000003	0.0141	0.000131	2359	0.90	2650	2960
ER21-50	0.282256	0.000012	0.0011	0.000028	0.0470	0.001280	464	−8.40	1408	2377
ER21-51	0.281194	0.000012	0.0005	0.000004	0.0203	0.000156	2449	−1.78	2829	3232
ER21-53	0.282350	0.000012	0.0005	0.000003	0.0201	0.000190	288	−8.70	1256	2281
ER21-54	0.281365	0.000013	0.0004	0.000005	0.0139	0.000181	2277	0.63	2590	2923
ER21-55	0.281332	0.000015	0.0005	0.000007	0.0181	0.000151	1976	−7.57	2645	3351
ER25-01	0.281936	0.000014	0.0005	0.000008	0.0153	0.000130	1700	7.76	1823	1954
ER25-02	0.281348	0.000016	0.0006	0.000010	0.0220	0.000095	1924	−8.24	2627	3368
ER25-06	0.281623	0.000012	0.0010	0.000022	0.0412	0.000766	1719	−3.49	2277	2854
ER25-08	0.281310	0.000013	0.0008	0.000022	0.0315	0.000913	2119	−5.55	2694	3293
ER25-10	0.281310	0.000012	0.0003	0.000005	0.0104	0.000165	2402	1.71	2655	2927
ER25-11	0.281636	0.000012	0.0007	0.000027	0.0279	0.001342	1676	−3.62	2241	2835
ER25-12	0.282527	0.000013	0.0005	0.000010	0.0179	0.000145	314	−1.85	1010	1748
ER25-13	0.281740	0.000014	0.0008	0.000023	0.0258	0.000625	1822	3.14	2108	2406
ER25-15	0.281387	0.000013	0.0013	0.000025	0.0537	0.001006	2378	2.22	2622	2870
ER25-16	0.282676	0.000013	0.0018	0.000016	0.0580	0.000456	267	2.18	831	1390
ER25-17	0.281382	0.000013	0.0008	0.000030	0.0353	0.001365	1859	−8.78	2597	3365
ER25-24	0.281384	0.000011	0.0002	0.000005	0.0088	0.000127	2359	3.44	2553	2762

Table A3. *Cont.*

Spot. No	$^{176}Hf/^{177}Hf$	1σ	$^{176}Lu/^{177}Hf$	1σ	$^{176}Yb/^{177}Hf$	1σ	Age (Ma)	εHf(t)	t_{DM1}	t_{DM2}
ER25-27	0.281319	0.000013	0.0005	0.000003	0.0180	0.000107	2174	−3.45	2656	3168
ER25-31	0.281355	0.000013	0.0012	0.000010	0.0461	0.000329	1990	−7.32	2659	3342
ER25-32	0.281347	0.000013	0.0003	0.000011	0.0131	0.000437	1851	−9.57	2610	3422
ER25-34	0.282310	0.000012	0.0006	0.000007	0.0217	0.000218	324	−9.36	1315	2359
ER25-35	0.281195	0.000013	0.0006	0.000014	0.0203	0.000575	2474	−1.19	2828	3203
ER25-38	0.281344	0.000013	0.0007	0.000033	0.0236	0.001245	2002	−6.67	2635	3300
ER25-39	0.281381	0.000013	0.0003	0.000004	0.0094	0.000068	1867	−7.92	2560	3303
ER25-40	0.281271	0.000012	0.0006	0.000004	0.0209	0.000105	2175	−5.32	2729	3315
ER25-41	0.281310	0.000014	0.0005	0.000003	0.0212	0.000193	2253	−2.06	2672	3116
ER25-43	0.281203	0.000013	0.0008	0.000007	0.0274	0.000254	2359	−3.85	2833	3329
ER25-49	0.282606	0.000012	0.0006	0.000012	0.0236	0.000626	305	0.71	905	1535
ER25-54	0.282658	0.000012	0.0009	0.000007	0.0320	0.000285	307	2.53	838	1390
ER25-59	0.281293	0.000012	0.0004	0.000002	0.0153	0.000132	2500	3.09	2689	2889
ER25-60	0.281390	0.000014	0.0004	0.000009	0.0120	0.000195	2386	4.06	2554	2733
ER25-61	0.281376	0.000013	0.0004	0.000009	0.0162	0.000147	1990	−5.49	2576	3199
ER25-65	0.282234	0.000015	0.0008	0.000048	0.0293	0.001779	432	−9.77	1428	2465
ER25-68	0.282180	0.000015	0.0007	0.000007	0.0255	0.000164	491	−10.37	1497	2553
ER50-04	0.281514	0.000012	0.0010	0.000009	0.0402	0.000297	1843	−4.71	2430	3036
ER50-05	0.281290	0.000015	0.0006	0.000028	0.0225	0.000807	2413	0.65	2707	3017
ER50-11	0.281340	0.000013	0.0009	0.000016	0.0347	0.000314	2236	−1.92	2656	3093
ER50-16	0.281310	0.000011	0.0008	0.000009	0.0354	0.000477	2313	−1.22	2695	3092
ER50-21	0.281291	0.000012	0.0003	0.000004	0.0123	0.000132	2540	4.11	2684	2838
ER50-23	0.281336	0.000012	0.0004	0.000013	0.0195	0.000664	2107	−4.32	2632	3190
ER50-26	0.282248	0.000012	0.0011	0.000019	0.0480	0.001115	443	−9.12	1419	2421
ER50-28	0.281280	0.000012	0.0003	0.000007	0.0115	0.000242	2363	−0.26	2696	3053
ER50-30	0.282482	0.000017	0.0007	0.000010	0.0254	0.000347	464	−0.25	1078	1723
ER50-35	0.281132	0.000012	0.0005	0.000007	0.0194	0.000275	2255	−8.34	2910	3605
ER50-39	0.281454	0.000011	0.0002	0.000007	0.0077	0.000317	2148	1.14	2458	2792
ER50-47	0.281392	0.000013	0.0005	0.000009	0.0182	0.000427	1927	−6.49	2562	3233
ER50-48	0.281454	0.000011	0.0012	0.000009	0.0351	0.000294	1841	−7.08	2523	3220
ER50-49	0.281299	0.000012	0.0005	0.000012	0.0178	0.000574	2416	1.34	2683	2966
ER50-55	0.282262	0.000013	0.0012	0.000012	0.0458	0.000477	343	−10.78	1404	2485
ER50-59	0.281441	0.000017	0.0007	0.000004	0.0247	0.000192	1849	−6.67	2504	3193
ER50-60	0.281708	0.000013	0.0028	0.000043	0.1286	0.001627	1785	−1.15	2266	2717
ER50-61	0.281092	0.000014	0.0008	0.000012	0.0302	0.000542	2380	−7.37	2985	3616
ER50-66	0.281288	0.000019	0.0014	0.000033	0.0491	0.000636	1948	−10.84	2762	3587
ER50-68	0.281309	0.000013	0.0005	0.000018	0.0182	0.000697	2419	1.65	2674	2944
ER50-71	0.281374	0.000013	0.0008	0.000019	0.0300	0.000489	2001	−5.87	2606	3237
ER50-76	0.281314	0.000017	0.0007	0.000007	0.0273	0.000249	2366	0.31	2681	3011

References

1. IAEA. *World Distribution of Uranium Deposits (UDEPO)*; IAEA-TECDOC-1843; International Atomic Energy Agency: Vienna, Austria, 2018; p. 262.
2. Cuney, M.; Mercadier, J.; Bonnetti, C. Classification of Sandstone-Related Uranium Deposits. *J. Earth Sci.* **2022**, *33*, 236–256. [CrossRef]
3. Ji, H.L.; He, Z.B.; Zhong, J.; Chen, H.; Zhu, B. Sedimentary Characteristics of Lower Cretaceous in Wuerhe–Huanghuagou Area, Northwestern Margin of Junggar Basin. *J. Ore Geol. Rev.* **2024**, *70*, 1267–1290.
4. Bonnetti, C.; Cuney, M.; Malartre, F.; Michels, R.; Liu, X.D.; Peng, Y.B. The Nuheting Deposit, Erlian Basin, NE China: Synsedimentary to Diagenetic Uranium Mineralization. *Ore Geol. Rev.* **2015**, *69*, 118–139. [CrossRef]
5. Bonnetti, C.; Cuney, M.; Michels, R.; Truche, L.; Malartre, F.; Liu, X.D.; Yang, J.X. The Multiple Roles of Sulfate-Reducing Bacteria and Fe-Ti Oxides in the Genesis of the Bayinwula Roll Front-Type Uranium Deposit, Erlian Basin, NE China. *Econ. Geol.* **2015**, *110*, 1059–1081. [CrossRef]
6. Bonnetti, C.; Liu, X.D.; Yan, Z.B.; Cuney, M.; Michels, R.; Malartre, F.; Mercadier, J.; Cai, J.F. Coupled Uranium Mineralisation and Bacterial Sulphate Reduction for the Genesis of the Baxingtu Sandstone-Hosted U Deposit, SW Songliao Basin, NE China. *Ore Geol. Rev.* **2017**, *82*, 108–129. [CrossRef]
7. Hou, B.; Keeling, J.L.; Li, Z. Paleovalley-Related Uranium Deposits in Australia and China: A Review of Geological and Exploration Models and Methods. *Ore Geol. Rev.* **2017**, *88*, 201–234. [CrossRef]
8. Zhang, X.; Nie, F.J.; Su, X.B.; Xia, F.; Li, M.G.; Yan, Z.B.; Zhang, C.Y.; Feng, Z.B. Relationships between Meso-Cenozoic Denudation in the Eastern Tian Shan and Uranium Mineralization in the Turpan-Hami Basin, NW China: Constraints from Apatite Fission Track Study. *Ore Geol. Rev.* **2020**, *127*, 103820.
9. Jin, R.S.; Teng, X.M.; Li, X.G.; Si, Q.H.; Wang, W. Genesis of sandstone-type uranium deposits along the northern margin of the Ordos Basin, China. *Geosci. Front.* **2020**, *11*, 215–227. [CrossRef]
10. Sun, D.; Xia, F.; Meng, F.M.; Nie, F.J.; Liu, X.; Zhang, W.W.; Wan, Q. Petrology of the Sandstone-Type Uranium Target Layer and Its Uranium Existence Form in the Telaaobao Mineral Area, Ordos Basin. *ACS Omega* **2025**, *10*, 912–928. [CrossRef] [PubMed]

11. Zhu, Q.; Li, J.G.; Wen, S.B.; Li, G.Y.; Yu, R.G.; Miao, P.S.; Zhang, B. Alteration, uranium occurrence state, and enrichment mechanism of the Cretaceous Luohe Formation, southwestern Ordos Basin, western China. *Ore Geol. Rev.* **2021**, *139*, 104496. [CrossRef]
12. Chen, Y.; Miao, P.S.; Li, J.G.; Jin, R.S.; Zhao, H.L.; Chen, L.L.; Wang, C.; Yu, H.Y.; Zhang, X.R. Association of Sandstone-Type Uranium Mineralization in the Northern China with Tectonic Movements and Hydrocarbons. *J. Earth Sci.* **2022**, *33*, 289–307. [CrossRef]
13. Khan, T.; Sarma, D.S.; Somasekhar, V.; Ramanaiah, S.; Reddy, N.R. Geochemistry of the Palaeoproterozoic quartzites of Lower-Cuddapah Supergroup, South India: Implications for the palaeoweathering, provenance, and crustal evolution. *Geol. J.* **2020**, *55*, 1587–1611. [CrossRef]
14. Khan, T.; Sarma, D.S.; Khan, M.S. Geochemical study of the Neoproterozoic clastic sedimentary rocks of the Khambal Formation (Sindreth Basin), Aravalli Craton, NW Indian Shield: Implications for paleoweathering, provenance, and geodynamic evolution. *Geochemistry* **2020**, *80*, 129956. [CrossRef]
15. Wanas, H.A.; Assal, E.M. Provenance, tectonic setting and source area-paleoweathering of sandstones of the Bahariya Formationin the Bahariya Oasis, Egypt: An implication to paleoclimate and paleogeography of the southern Neo-Tethys region duringEarly Cenomanian. *Sediment. Geol.* **2021**, *413*, 105822. [CrossRef]
16. Li, Y.; Nie, F.J.; Jia, L.C.; Lu, S.J.; Yan, Z.B. Geochemical Characteristics, Palaeoenvironment and Provenance of Uranium-BearingSandstone in the Sifangtai Formation, Northern Songliao Basin, Northeast China. *Minerals* **2021**, *11*, 1019. [CrossRef]
17. Huang, G.W.; Pan, J.Y.; Xia, F.; Yan, J.; Zhang, C.Y.; Wu, D.H.; Liu, Y. Provenance of uranium mineralization of the Yuqia area, Northwest China: Constraints from detrital zircon U-Pb geochronology and Hf isotopes. *J. Earth Sci.* **2022**, *33*, 1549–1570. [CrossRef]
18. Huang, G.W.; Wu, D.H.; Huang, G.N.; Xue, W.W.; Min, Z.; Fan, P.F. Provenance of Jurassic sediments from Yuqia sandstonetype uranium deposits in the Northern margin of Qaidam Basin, China and its implications for uranium mineralization. *Minerals* **2022**, *12*, 82. [CrossRef]
19. Sun, Y.H.; Jiao, Y.Q.; Cuney, M.; Wu, L.Q.; Mercadier, J.; Rong, H.; Liu, Y.; Tao, Z.P. Sulfur Isotope and Trace Element Constraints on the Conditions of Pyrite Formation from the Diantou-Shuanglong Sandstone-Hosted Uranium Deposit, Ordos Basin, China: Implications for Uranium Mineralization. *Ore Geol. Rev.* **2024**, *165*, 105921. [CrossRef]
20. Liu, C.Y.; Zhang, L.; Huang, L.; Wu, B.L.; Wang, J.Q.; Zhang, D.D.; Tan, C.Q.; Ma, Y.P.; Zhao, J.S. Novel Metallogenic Model of Sandstone-Type Uranium Deposits: Mineralization by Deep Organic Fluids. *Earth Sci. Front.* **2024**, *31*, 368–383.
21. Wang, F.F.; Liu, C.Y.; Niu, H.Q.; Zhou, N.C.; Li, X.H.; Luo, W.; Zhang, D.D.; Zhao, Y. In-Situ Chemical Age of the Sandstone-Hosted Uranium Deposit in Ningdong Area on the Western Margin of the Ordos Basin, North China. *J. Acta Geol. Sin.* **2018**, *92*, 406–407. [CrossRef]
22. Zhang, J.D.; Xu, G.Z.; Lin, J.R.; Peng, Y.B.; Wang, G. The Implication of Six Kinds of New Sandstone-Type Uranium Deposits to Uranium Resources Potential in North China. *Geol. China* **2010**, *37*, 1434–1449.
23. Wu, Z.Q.; Hu, Y.X.; Liu, K.P.; Wang, X.P.; Liu, C.H.; Wang, K.; Zhang, L.; Pan, J.Y.; Mao, N.; Wang, Q.H. Basic Feature of Mineralization Host Rocks and Its Relation to Uranium Metallogenesis in Zhenyuan, Southern Ordos Basin. *Uranium Geol.* **2023**, *39*, 960–969.
24. Sun, D.; Li, H.; Xia, F.; Nie, F.J.; Huang, G.W.; Zhang, Z.B.; Meng, F.M.; Pan, J.Y.; Hu, Y.J. Provenance and Tectonic Setting of the Lower Cretaceous Huanhe Formation in the Northwestern Ordos Basin and Its Implications for Uranium Mineralization. *ACS Omega* **2024**, *9*, 3324–3341. [CrossRef]
25. Liu, H.B.; Li, Z.Y.; Qin, M.K.; Sun, Y.; Han, J.; Jin, G.S.; Li, J.J. Advances in Geochemistry of Sandstone-Hosted Uranium Deposits in the Northern Ordos Basin. *Earth Sci. Front.* **2012**, *19*, 139–146.
26. Wu, B.L.; Zhang, W.Y.; Song, Z.S.; Cun, X.N.; Sun, L.; Luo, J.J.; Li, Y.Q.; Cheng, X.H.; Sun, B. Geological and Geochemical Characteristics of Uranium Minerals in Sandstone-Type Uranium Deposits of the Northern Ordos Basin and Their Genetic Significance. *Acta Geol. Sin.* **2016**, *90*, 3393–3407.
27. Weltje, G.J.; Eynatten, H.V. Quantitative Provenance Analysis of Sediments: Review and Outlook. *Sediment. Geol.* **2004**, *171*, 1–11. [CrossRef]
28. Hietpas, J.; Samson, S.; Moecher, D.; Chakraborty, S. Enhancing Tectonic and Provenance Information from Detrital Zircon Studies: Assessing Terrane-Scale Sampling and Grain-Scale Characterization. *J. Geol. Soc.* **2011**, *168*, 309–318. [CrossRef]
29. Luo, X.; Li, Z.; Cai, Y.; Yi, C.; Zhang, Z.; Zhang, Y.; Zhang, Y. Provenance and Tectonic Setting of Lower Cretaceous Huanhe Formation Sandstones, Northwest Ordos Basin, North-Central China. *Minerals* **2021**, *11*, 1376. [CrossRef]
30. Li, S.T.; Lin, C.S.; Xie, X.N.; Yang, S.G.; Jiao, Y.Q. Approaches of Nonmarine Sequence Stratigraphy—A Case Study on the Mesozoic Ordos Basin. *Sediment. Geol.* **1995**, *2*, 133–148.
31. Shi, W.; Dong, S.W.; Hu, J.M. Neotectonics around the Ordos Block, North China: A Review and New Insights. *Earth-Sci. Rev.* **2020**, *200*, 102969. [CrossRef]

32. Chen, A.Q.; Zou, H.; Ogg, J.G.; Yang, S.; Hou, M.C.; Jiang, X.W.; Xu, S.L.; Zhang, X.X. Source-to-Sink of Late Carboniferous Ordos Basin: Constraints on Crustal Accretion Margins Converting to Orogenic Belts Bounding the North China Block. *Geosci. Front.* **2020**, *11*, 2031–2052. [CrossRef]
33. Zhong, W.H.; Wu, L.Q.; Wang, L.H.; Jiao, Y.Q.; Zhang, F.; Yue, L.; Xiang, Y.; Zheng, Y.H. The Distinctiveness of Carbonaceous Debris in Uranium Reservoirs under Arid Sedimentary Backgrounds and Its Implication for Uranium Mineralization: A Case Study of Northern Ordos Basin. *Ore Geol. Rev.* **2025**, *179*, 106526. [CrossRef]
34. Wang, L.H.; Yan, P.B.; Jiao, Y.Q.; Wu, L.Q.; Zhang, Z.L.; Rong, H.; Zhang, F.; Li, Z.C.; Zhong, W.H. Uranium Metallogenic Model of Lower Cretaceous in Northern Ordos Basin. *J. Bull. Geol. Sci. Technol.* **2023**, *42*, 222–233.
35. Meng, Q.R.; Wu, G.L.; Fan, L.G.; Wei, H.H. Tectonic Evolution of Early Mesozoic Sedimentary Basins in the North China Block. *Earth-Sci. Rev.* **2019**, *190*, 416–438. [CrossRef]
36. Deng, J.; Wang, Q.F.; Gao, B.F.; Xu, H.; Zhou, Y.H. Distribution and Tectonic Background of Various Energy Resources in Ordos Basin. *Earth Sci. J. China Univ. Geosci.* **2006**, *3*, 330–336.
37. Hu, Y.X.; Yang, T.; Zhang, X.; Ou, Y.J.; Liu, Z.R.; Si, H.J.; Li, X.Q. Carbon and Oxygen Isotope Characteristics and Uranium Metallogenic Significance of Sandstone-type Uranium Deposits in the Lower Cretaceous Luohe Formation in Zhenyuan Area, Southern Ordos Basin. *Geoscience* **2025**, *166*, 105937. (In Chinese with English abstract)
38. Ju, Y.; Wang, W.; Ren, Z.; Yang, Z.; Liu, K.; Hou, B.; Xiao, L. Multi-Stage Evolution of the Ordos Basin: Its Coupled Basin-Mountain Systems and Energy Resources. *Sci. China Earth Sci.* **2025**, *68*, 2426–2473. [CrossRef]
39. Chen, R.; Wang, F.; Li, Z.; Evans, N.J.; Chen, H.D.; Wei, X.S. Late Paleozoic Provenance Shift in the East-Central Ordos Basin: Implications for the Tectonic Evolution of the North China Craton. *J. Asian Earth Sci.* **2021**, *215*, 104799. [CrossRef]
40. Dong, Y.P.; Hui, B.; Sun, S.X.; Yang, Z.; Zhang, F.F.; He, D.F.; Sun, J.P.; Shi, X.H. Multiple Orogeny and Geodynamics from Proto-Tethys to Paleo-Tethys of the Central China Orogenic Belt. *Acta Geol. Sin.* **2022**, *96*, 3426–3448. (In Chinese with English abstract)
41. Wang, Z.W.; Liu, L.; Hu, J.L.; Wang, F.; Li, D.; Zhang, J.Q.; Zhu, S.Y.; Zhang, R.; Zhao, F.; Zhang, C.G.; et al. Dispersion of Sandy Sediments During Marine–Continental Transition: An Integrated Study from the Late Paleozoic Western Ordos Basin. *Mar. Pet. Geol.* **2024**, *160*, 106620. [CrossRef]
42. Wang, G.; Liu, B.; Bai, Y.M.; Wang, L.H.; Li, H.M.; Lu, S.S. Geological Characteristics and Metallogenic Mechanism of Lower Cretaceous Uranium Mineralization in Northern Ordos Basin. *World Nucl. Geosci.* **2025**, *42*, 485–503. (In Chinese)
43. Jiao, Y.Q.; Wu, L.Q.; Rong, H.; Zhang, F. Coal Accumulation Regularity of Zhiluo Formation and Its Indication to Paleoclimate and Uranium Metallogenic Environment, Ordos Basin. *J. China Coal Soc.* **2021**, *46*, 2331–2345.
44. *NIST SRM 1646a*; Estuarine Sediment Standard. National Institute of Standards and Technology: Gaithersburg, MD, USA, 2010.
45. *GSD-12*; Shale Standard. Institute of Geophysical and Geochemical Exploration, Chinese Academy of Geological Sciences: Langfang, China, 2008.
46. *ISO 11466:1995*; Soil Quality—Extraction of Trace Elements Soluble in Aqua Regia. ISO: Geneva, Switzerland, 1995.
47. *SRM 610*; Trace Elements in Glass. National Institute of Standards and Technology: Gaithersburg, MD, USA, 1972.
48. McDonough, W.F.; Sun, S.-S. The Composition of the Earth. *Chem. Geol.* **1995**, *120*, 223–253. [CrossRef]
49. Dan, W.; Li, X.H.; Guo, J.H.; Liu, Y.; Wang, X.C. Integrated in situ Zircon U-Pb Age and Hf-O Isotopes for the Helanshan Khondalites in North China Craton: Juvenile Crustal Materials Deposited in Active or Passive Continental Margin? *Precambrian Res* **2012**, *222–223*, 143–158. [CrossRef]
50. Yin, C.Q.; Zhao, G.C.; Guo, J.H.; Sun, M.; Xia, X.P.; Zhou, X.W.; Liu, C.H. U-Pb and Hf Isotopic Study of Zircons of the Helanshan Complex: Constraints on the Evolution of the Khondalite Belt in the Western Block of the North China Craton. *Lithos* **2011**, *122*, 25–38. [CrossRef]
51. Xi, X.P.; Sun, M.; Zhao, G.C.; Wu, F.Y.; Xu, P.; Zhang, J.; He, Y.H. Paleoproterozoic Crustal Growth in the Western Block of the North China Craton: Evidence from Detrital Zircon Hf and Whole Rock Sr-Nd Isotope Compositions of the Khondalites in the Jining Complex. *Am. J. Sci.* **2008**, *308*, 304–327. [CrossRef]
52. Ma, X.D.; Guo, J.H.; Liu, F.; Qian, Q.; Fan, H.R. Zircon U-Pb Ages, Trace Elements and Nd-Hf Isotopic Geochemistry of Guyang Sanukitoids and Related Rocks: Implications for the Archean Crustal Evolution of the Yinshan Block, North China Craton. *Precambrian Res.* **2013**, *230*, 61–78. [CrossRef]
53. Ma, M.Z.; Xu, Z.Y.; Zhang, L.C.; Dong, C.Y.; Dong, X.J.; Liu, S.J.; Liu, D.Y.; Wan, Y.S. SHRIMP Dating and Hf Isotope Analysis of Zircons from the Early Precambrian Basement in the Xi Ulanbulang Area, Wuchuan, Inner Mongolia. *Acta Petrol. Sin.* **2013**, *29*, 501–516.
54. Wang, D.; Guo, J.H.; Huang, G.Y.; Scheltens, M. The Neoarchean Ultramafic-Mafic Complex in the Yinshan Block, North China Craton: Magmatic Monitor of Development of Archean Lithospheric Mantle. *Precambrian Res.* **2015**, *270*, 80–99. [CrossRef]
55. Li, X.P.; Wang, H.; Kong, F.M. Probe into the genesis of high temperature-ultrahigh temperature metamorphism: The enlightenment from the Western Khondalite Belt of the North China Craton and the Namaqua mobile belt and the Bushveld metamorphic complex of South Africa. *Acta Petrol. Sin.* **2019**, *35*, 295–311. (In Chinese with English abstract)

56. Ma, X.C.; Liu, L.; Wang, Z.W.; Hu, A.P.; Hu, J.L.; Hu, C.; Wang, F.; Li, D.; Zhang, C.G.; Fu, S.Y.; et al. Detrital Material Source and Paleogeographic Reconstruction of Taiyuan Formation in Western Ordos Basin [J/OL]. *Acta Sedimentol. Sin.* **2025**, 1–23. (In Chinese with English abstract) [CrossRef]
57. Zhai, M.G.; Santosh, M. The Early Precambrian Odyssey of the North China Craton: A Synoptic Overview. *Gondwana Res.* **2011**, *20*, 6–25. [CrossRef]
58. Zhai, M.G.; Santosh, M.; Zhang, L. Precambrian Geology and Tectonic Evolution of the North China Craton. *Gondwana Res.* **2011**, *20*, 1–5. [CrossRef]
59. Wang, M.; Luo, J.L.; Li, M.; Bai, X.J.; Cheng, C.; Yan, L.W. Provenance and Tectonic Setting of Sandstone-Type Uranium Deposit in Dongsheng Area, Ordos Basin: Evidence from U-Pb Age and Hf Isotopes of Detrital Zircons. *Acta Petrol. Sin.* **2013**, *29*, 2746–2758.
60. Zhao, G.C.; Wilde, S.A.; Cawood, P.A. Tectonothermal History of the Basement Rocks in the Western Zone of the North China Craton and Its Tectonic Implications. *Tectonophysics* **1999**, *310*, 37–53. [CrossRef]
61. Zhao, G.C.; Cawood, P.A.; Wilde, S.A.; Min, S.; Lu, L.Z. Metamorphism of Basement Rocks in the Central Zone of the North China Craton: Implications for Paleoproterozoic Tectonic Evolution. *Precambrian Res.* **2000**, *103*, 55–88. [CrossRef]
62. Wang, H.C.; Yuan, G.B.; Xin, H.T. U-Pb Single Zircon Ages for Granulites in Cunkongshan Area, Guyang Inner Mongolia and Enlightenment for Its Geological Signification. *Prog. Precambrian Res.* **2001**, *24*, 28–34.
63. Zhang, W.J.; Li, L.; Geng, M.S. Petrology and Dating of Neo-Archaean Intrusive Rocks from Guyang Area, Inner Mongolia. *Earth Sci.* **2000**, *25*, 221–226.
64. Wu, C.H.; Sun, M.; Li, H.M.; Zhao, G.C.; Xia, X.P. LA-ICP-MS U-Pb Zircon Ages of the Khondalites from the Wulashan and Jining High-Grade Terrain in Northern Margin of the North China Craton: Constraints on Sedimentary Age of the Khondalite. *Acta Petrol. Sin.* **2006**, *22*, 2639–2654.
65. Shi, Q.; Ma, L.; Chen, X.Z.; Xu, Z.Y.; Li, S.C. Discovery of ca. 2.5 Ga Charnockite in the Daqing Mountains: Implications for the Petrogenetic Model of Anatectic Garnet Granite. *Geol. Rev.* **2024**, *70*, 1139–1144.
66. Dong, C.Y.; Liu, D.Y.; Li, J.J.; Wan, Y.S.; Zhou, H.Y.; Li, C.D.; Yang, Y.H.; Xie, L.W. New Evidence for the Formation Age of the Khondalite Belt in the Western North China Craton: Zircon SHRIMP Dating and Hf Isotopic Compositions from the Bayan Wula-Helan Mountains Region. *Sci. Bull.* **2007**, *16*, 1913–1922.
67. Dong, C.Y.; Liu, D.Y.; Wan, Y.S.; Xu, Z.Y.; Wang, W.; Jie, H.Q. Hf Isotope Composition and REE Pattern of Zircons from Early Precambrian Metamorphic Rocks in the Daqing Mountains, Inner Mongolia. *Geol. Rev.* **2009**, *55*, 509–520.
68. Zhong, C.T.; Deng, J.F.; Wan, Y.S.; Mao, D.B.; Li, H.M. Magma Recording of Paleoproterozoic Orogeny in Central Segment of Northern Margin of North China Craton: Geochemical Characteristics and Zircon SHRIMP Dating of S-Type Granitoids. *Geochimica* **2007**, *36*, 585–600.
69. Liu, S.J.; Dong, C.Y.; Xu, Z.Y.; Santosh, M.; Ma, M.Z.; Xie, H.Q.; Liu, D.Y.; Wan, Y.S. Palaeoproterozoic Episodic Magmatism and High-Grade Metamorphism in the North China Craton: Evidence from SHRIMP Zircon Dating of Magmatic Suites in the Daqingshan Area. *Geol. J.* **2013**, *48*, 429–455. [CrossRef]
70. Wang, X.; Zhang, J.; Yin, C.Q.; Liu, X.G.; Chen, Y.; Cheng, C.Q.; Guo, M.J. Petrogenesis and Tectonic Implications of 1.86–1.80 Ga A-Type Granites in the Daqingshan Complex, Khondalite Belt, North China Craton. *Precambrian Res.* **2022**, *378*, 106757. [CrossRef]
71. Xu, C.H.; Sun, F.Y.; Fan, X.Z.; Li, L.; Liu, J.L.; Yu, L. Late Paleoproterozoic Crustal Evolution in the Daqingshan Area: Evidences from Adakitic and A-Type Granitoids in the Guyang Changshengqu Goldfield, Khondalite Belt, North China Craton. *Precambrian Res.* **2020**, *345*, 105761. [CrossRef]
72. Chen, L.; Cheng, C.; Wei, Z. Seismic Evidence for Significant Lateral Variations in Lithospheric Thickness Beneath the Central and Western North China Craton. *Earth Planet. Sci. Lett.* **2009**, *286*, 171–183. [CrossRef]
73. Xu, B.; Wang, Z.W.; Zhang, L.Y.; Wang, Z.H.; Yang, Z.N.; He, Y. The Xing-Meng Intracontinent Orogenic Belt. *Acta Petrol. Sin.* **2018**, *34*, 2819–2844.
74. Luo, H.L.; Wu, T.R.; Zhao, L.; He, Y.K.; Jin, X. Permian High Ba-Sr Granitoids: Geochemistry, Age and Tectonic Implications of Erlangshan Pluton, Urad Zhongqi, Inner Mongolia. *Acta Geol. Sin.* **2009**, *83*, 603–614. [CrossRef]
75. Luo, H.L.; Wu, T.R.; Zhao, L. Zircon SHRIMP U-Pb Dating of Wuliangsitai A-Type Granite on the Northern Margin of the North China Plate and Tectonic Significance. *Acta Petrol. Sin.* **2009**, *25*, 515–526.
76. Liu, C.F.; Liu, W.C.; Zhou, Z.G. Geochronology, Geochemistry and Tectonic Setting of the Paleozoic–Early Mesozoic Intrusive in Siziwangqi, Inner Mongolia. *Acta Geol. Sin.* **2014**, *88*, 992–1002. [CrossRef]
77. Dong, C.Y.; Wan, Y.S.; Wilde, S.A.; Xu, Z.Y.; Ma, M.Z.; Xie, H.Q.; Liu, D.Y. Earliest Paleoproterozoic Supracrustal Rocks in the North China Craton: Recognized from the Daqingshan Area of the Khondalite Belt: Constraints on Craton Evolution. *Gondwana Res.* **2014**, *25*, 1535–1553. [CrossRef]
78. Ma, M.Z.; Wan, Y.S.; Santosh, M.; Xu, Z.Y.; Xie, H.Q.; Dong, C.Y.; Liu, D.Y.; Guo, C.L. Decoding Multiple Tectonothermal Events in Zircons from Single Rock Samples: SHRIMP Zircon U-Pb Data from the Late Neoproterozoic Rocks of Daqingshan, North China Craton. *Gondwana Res.* **2012**, *22*, 810–827. [CrossRef]

79. Dan, W.; Li, X.H.; Guo, J.H.; Liu, Y.; Wang, X.C. Paleoproterozoic Evolution of the Eastern Alxa Block, Westernmost North China: Evidence from in situ Zircon U–Pb Dating and Hf–O Isotopes. *Gondwana Res.* **2012**, *21*, 838–864. [CrossRef]
80. Dan, W.; Li, X.H.; Wang, Q.; Wang, X.C.; Liu, Y.; Wyman, D.A. Paleoproterozoic S-Type Granites in the Helanshan Complex, Khondalite Belt, North China Craton: Implications for Rapid Sediment Recycling During Slab Break-Off. *Precambrian Res.* **2014**, *254*, 59–72. [CrossRef]
81. Zhai, M.G. Tectonic Evolution of the North China Craton. *J. Geomech.Geophys.* **2019**, *25*, 722–745.
82. Zhai, M.G.; Zhao, L.; Zhu, X.Y.; Zhou, Y.Y.; Peng, P.; Guo, J.H.; Li, Q.L.; Zhao, T.P.; Lu, J.S.; Li, X.H. Late Neoarchean Magmatic-Metamorphic Event and Crustal Stabilization in the North China Craton. *Am. J. Sci.* **2021**, *321*, 206–234. [CrossRef]
83. Zhai, M.G.; Peng, P. Paleoproterozoic Events in the North China Craton. *Acta Petrol. Sin.* **2007**, *23*, 2665–2682.
84. Huang, B.; Kusky, T.M.; Johnson, T.E.; Wilde, S.A.; Wang, L.; Polat, A.; Fu, D. Paired Metamorphism in the Neoarchean: A Record of Accretionary-to-Collisional Orogenesis in the North China Craton. *Earth Planet. Sci. Lett.* **2020**, *543*, 116355. [CrossRef]
85. Yang, T.X.; Yu, R.G.; Rong, H.; Li, T.; Zhu, Q. Geochemistry of Sandstones and U-Pb Ages of Detrital Zircons in the Zhiluo Formation of the Central and Northern Ordos Basin, China: Constraints on Provenance and Tectonic Setting. *Acta Geosci. Sin.* **2024**, *45*, 941–952.
86. Zhang, S.H.; Zhao, Y.; Liu, J.; Hu, J.M.; Chen, Z.L.; Li, M.; Pei, J.L.; Chen, Z.Y.; Zhou, J.X. Emplacement Depths of the Late Paleozoic-Mesozoic Granitoid Intrusions from the Northern North China Block and Their Tectonic Implications. *Acta Petrol. Sin.* **2007**, *23*, 625–638.
87. Zhang, N.; Wang, C.B.; Liu, Z.H.; Xu, Z.Y.; Li, G.; Xuan, Y.F.; Gao, Y.; Wang, C. Tectonic Evolution of the Late Paleozoic-Early Mesozoic Orogenic Belt in the Eastern Segment of the Northern Margin of the North China Block: Evidence from Meta-Volcanic Rocks of Jianshanzi, Northern Liaoning Province. *Acta Petrol. Sin.* **2022**, *38*, 2323–2344.
88. Ren, Z.L.; Qi, K.; Liu, R.C.; Cui, J.P.; Chen, Z.P. Dynamic Background of Early Cretaceous Tectonic Thermal Events and Its Control on Various Mineral Accumulations Such as Oil and Gas in the Ordos Basin. *Acta Petrol. Sin.* **2020**, *36*, 1213–1234. (In Chinese)
89. He, X.Y.; Liu, C.Y.; Zhang, L.; Wang, J.Q.; Huang, L.P.; Du, F.P.; Yang, X.K. The Tectonic Uplift Episodes and Energy Effects in the Northeastern Ordos Basin. *Acta Geol. Sin.* **2024**, *98*, 3735–3750.
90. Wan, T.F. Discussion on the Liupanshan-Helanshan Collision Zone. *Geotecton. Metallog.* **2020**, *44*, 845–851. (In Chinese with English abstract)
91. Zhao, H.L.; Zang, Y.L.; Li, J.G.; Zhang, B.; Chen, L.L. Preliminary Study on the Occurrence State of Uranium in the Lower Cretaceous Luohe Formation of Pengyang Uranium Deposit, Southwestern Ordos Basin. *North China Geol.* **2022**, *45*, 21–27. (In Chinese with English abstract)
92. Ren, Y.S.; Yang, X.Y.; Miao, P.S.; Hu, X.W.; Chen, Y.; Chen, L.L.; Zhao, H.L. Mineralogical and Geochemical Research on Pengyang Deposit: A Peculiar Eolian Sandstone-Hosted Uranium Deposit in the Southwest of Ordos Basin. *Ore Geol. Rev.* **2022**, *141*, 104571. [CrossRef]
93. Taylor, S.R.; McLennan, S.M. *The Continental Crust: Its Composition and Evolution*; Blackwell Scientific Publications: Oxford, UK, 1985.
94. Cullers, R.L. The Controls on the Major- and Trace-Element Evolution of Shales, Siltstones and Sandstones of Ordovician to Tertiary Age in the Wet Mountains Region, Colorado, USA. *Chem. Geol.* **1995**, *123*, 107–131. [CrossRef]
95. Hou, W.; Liu, Z.J.; Wang, W.T.; He, Y.P.; Zhang, W. REE Geochemical Characteristics of the Lower Cretaceous Mudstone in Suibin Depression of Eastern Heilongjiang Province. *J. Palaeogeogr.* **2007**, *9*, 207–215. (In Chinese with English abstract)
96. Bao, H.Y.; Yang, F.L.; Wang, D.P. Geochemical Characteristics of Sedimentary Rock in Southern Jiangsu Province on Mesozoic and Paleozoic: A Perspective from the SK-1 Well. *J. Jilin Univ.: Earth Sci. Ed.* **2011**, *41* (Suppl. 1), 29–38. (In Chinese with English abstract)
97. Diwu, C.R. Crustal Growth and Evolution of Archean Continental Crust in the Southern North China Craton. *Acta Petrol. Sin.* **2021**, *37*, 317–340.
98. Liu, S.; Feng, C.X.; Hu, R.Z.; Feng, G.Y.; Yu, X.F.; Li, C.; Jia, D.C.; Qi, Y.Q. Zircon U-Pb Age and Hf Isotope Characteristics of the Hercynian Granite in the Eastern Jilin Province and the Crustal Growth. *Acta Petrol. Sin.* **2012**, *28*, 3715–3720.
99. Liu, R.; Yang, Z.; Xu, Q.D.; Zhang, X.J.; Yao, C.L. Zircon U-Pb Ages, Elemental and Sr-Nd-Pb Isotopic Geochemistry of the Hercynian Granitoids from the Southern Segment of the Da Hinggan Mts.: Petrogenesis and Tectonic Implications. *Acta Petrol. Sin.* **2016**, *32*, 1505–1528.
100. Amirdin, A.; Xie, G.A.; Zhang, J.; Qu, J.F.; Tian, R.S.; Zhao, H.; Li, F.H.; Li, T. Geochemistry, Zircon U-Pb Age and Tectonic Settings of Pillow Basalts in the Langshan Area on the Northern Margin of the Alxa Block, Inner Mongolia. *Geol. Bull. China* **2019**, *38*, 810–823.
101. Zhang, F.C. Geochronology, Geochemistry and Geological Significance of the Xiaodaqingshan Granites in Jining, Inner Mongolia. Master's Thesis, China University of Geosciences, Beijing, China, 2019.
102. Chang, Z.G. Petrogenesis and Geological Significance of Mesozoic Bainuyangpan Formation Volcanic Rocks in Yinshan Area, Inner Mongolia. Master's Thesis, Taiyuan University of Technology, Taiyuan, China, 2017.

103. Wang, W.L.; Teng, X.J.; Liu, Y.; Teng, F.; Guo, S.; He, P.; Tian, J.; Duan, X.L. Zircon U-Pb Chronology and Geochemical Characteristics of the Wuheertu Granite Mass in Langshan, Inner Mongolia. *J. Geomech.Geophys.* **2017**, *23*, 15–25.
104. Hui, J.; Fan, L.Y.; Zhao, W.B.; Kang, R.; Wang, Y.F.; Zhang, J.; Zhang, B.H.; Zhao, H. Late Triassic Extension in the Northwestern Ordos Basin: Constraints from Langshan Basalts, NW China. *Acta Geol. Sin.* **2024**, *98*, 1–15.
105. Tian, J.; Teng, X.J.; Liu, Y.; Teng, F.; Guo, S.; He, P.; Wang, W.L. Chronology and Geochemistry of the Early Permian Granodiorite in Langshan Area, Inner Mongolia and Its Tectonic Setting. *Geol. China* **2020**, *47*, 767–781.
106. Zhao, C.; Wang, X.; Liu, J.; Zhang, J.; Chen, J.S.; Zhang, C.; Cui, D.D.; Cui, Y.S. Zircon U-Pb-Hf Isotopes and Geochemistry of Neoarchean TTG Gneisses in the Guyang Area of the Yinshan Block: Constraints on Petrogenesis and Tectonic Implications. *Acta Petrol. Sin.* **2024**, *40*, 3465–3483. [CrossRef]
107. Wu, B. Neoarchean Felsic Magmatism in the Guyang Area of the North China Craton and Its Implications for Early Plate Tectonics. Ph.D. Thesis, Northwest University, Xi'an, China, 2022.
108. Zhang, S.C.; Liu, P.; Ji, B.J. Thorium Resources and Their Availability. *World Nucl. Geosci.* **2005**, *22*, 98–103.
109. Wang, X.; Griffin, W.L.; Chen, J.; Huang, P.Y.; Li, X. U and Th Contents and Th/U Ratios of Zircon in Felsic and Mafic Magmatic Rocks: Improved Zircon-Melt Distribution Coefficients. *Acta Geol. Sin.* **2011**, *85*, 164–174.
110. Wang, W.Q.; Liu, C.Y.; Wang, J.Q.; Ma, H.H.; Guan, Y.Z. Characteristics of Uranium Content and Its Geological and Mineralization Significance for the Provenance Areas, Northern Northwest China. *Earth Sci. Front.* **2019**, *26*, 292–303. (In Chinese with English abstract)
111. Feng, Z.B.; Zhang, B.C.; Nie, F.J.; Xia, F.; Ning, J.; Zhang, L.L. Characteristics of rock fissure fillings and their relationship with the accumulation of uranium and associated elements in the Kailu Sag of southern Songliao Basin, Northeast China. *Ore Geol. Rev.* **2024**, *169*, 106079. [CrossRef]
112. Peng, H.; Jiao, Y.Q.; Fu, X.F.; Wu, L.Q.; Guo, X.D.; Wang, Q.S.; Liu, C. Provenance and uranium source tracing for uranium-bearing series in the south of Songliao Basin: Evidence from zircon U–Pb chronology and lithogeochemistry. *J. Geochem. Explor.* **2025**, *272*, 107703. (In Chinese with English abstract) [CrossRef]
113. Cheng, Y.H.; Petrov, V.; Jin, R.S.; Miao, P.S. Neotectonic controls on large-scale uranium mineralization in the Meso-Cenozioc basins, Northern China. *Ore Geol. Rev.* **2025**, *176*, 106393. [CrossRef]
114. Peng, H.; Jiao, Y.Q.; Dong, F.S.; Guo, X.D. Relationships between uranium occurrence, pyrite and carbonaceous debris in Fuxin Formation in the Songliao Basin: Evidenced by mineralogy and sulfur isotopes. *Ore Geol. Rev.* **2022**, *140*, 104580. [CrossRef]
115. Huang, H.; Cawood, P.A.; Ni, S.J.; Hou, M.C.; Shi, Z.Q. Provenance of late Paleozoic strata in the Yili Basin: Implications for tectonic evolution of the South Tianshan orogenic belt. *Geol. Soc. Am. Bull.* **2018**, *130*, 952–974. [CrossRef]
116. Huang, G.W.; Xue, W.W.; Pan, J.Y.; Song, T.Z.; Huang, G.N.; Zhang, C.Y.; Bai, X.D.; Zhang, T.; Hong, B.Y. Provenance and Tectonic Setting of Sandstones in the Mengqiguer Sandstone-type Uranium Deposit, Yili Basin: Evidence from Zircon U-Pb Chronology. *Geotecton. Metall.* **2018**, *42*, 1108–1141.
117. Zhang, X.; Nie, F.J.; Xia, F.; Zhang, C.Y.; Feng, Z.B. Provenance constraints on the Xishanyao Formation, southern Yili Basin, northwest China: Evidence from petrology, geochemistry, and detrital zircon U–Pb geochronology. *Can. J. Earth Sci.* **2018**, *55*, 1020–1035. [CrossRef]

Disclaimer/Publisher's Note: The statements, opinions and data contained in all publications are solely those of the individual author(s) and contributor(s) and not of MDPI and/or the editor(s). MDPI and/or the editor(s) disclaim responsibility for any injury to people or property resulting from any ideas, methods, instructions or products referred to in the content.